Article:

Yamasaki, T, Takahashi, H, Ohzono, M et al. (2 more authors) (2021) The influence of elastic thickness non-uniformity on viscoelastic crustal response to magma emplacement: application to the Kutcharo caldera, eastern Hokkaido, Japan. Geophysical Journal International, 224 (1). pp. 701-718. ISSN 0956-540X

https://doi.org/10.1093/gji/ggaa440

The influence of elastic thickness non-uniformity on viscoelastic crustal response to magma emplacement: Application to the Kutcharo caldera, eastern Hokkaido, Japan

Tadashi Yamasaki[1]*, Hiroaki Takahashi[2], Mako Ohzono[2,3], Tim J. Wright[4], and Tomokazu Kobayashi[5]

[1]Geological Survey of Japan, AIST, 1-1-1 Higashi, Tsukuba, Ibaraki 305-8567, Japan
[2]Institute of Seismology and Volcanology, Faculty of Science, Hokkaido University, N10W8, Kita-ku, Sapporo, Hokkaido 060-0810, Japan
[3]Earthquake Research Institute, The University of Tokyo, 1-1-1 Yayoi, Bunkyo-ku, Tokyo 113-0032, Japan
[4]COMET, School of Earth and Environment, University of Leeds, Leeds, LS2 9JT, United Kingdom
[5]Geospatial Information Authority of Japan, 1 Kitasato, Tsukuba, Ibaraki 305-0811, Japan

* All correspondence concerning this paper should be addressed to:
Tadashi Yamasaki
Geological Survey of Japan, AIST
1-1-1 Higashi, Tsukuba, Ibaraki 305-8567, Japan
Phone: +81-(0)29-861-3697
Fax: +81-(0)29-856-8725
Email: tadashi.yamasaki@aist.go.jp

SUMMARY

An elastic layer plays an important role in deformation of the crust. At active volcanoes, its thickness would be effectively thinned by a higher geothermal gradient, particularly in a region beneath which magmatic activity is relatively high. This study examines the influence of elastic thickness non-uniformity on viscoelastic crustal deformation by magma emplacement. A 3-D linear Maxwell viscoelastic model is employed, in which an elastic layer underlain by a viscoelastic layer with a spatially uniform viscosity is thinned to be h_i in the volcano centre, compared with $h_i + \Delta h$ in the peripheral regions, and a sill-like magma emplacement occurs in the upper layer beneath the centre. It is found that the post-emplacement viscoelastic subsidence is diminished or enhanced by the elastic thickness non-uniformity, depending on whether or not the horizontal width of the magma emplacement (ω_s) is greater than the horizontal width (ω_e) over which the elastic layer is thinner. The available signature of the non-uniformity is explored by comparison with a model that has a spatially uniform elastic thickness of h_i. If an apparent viscosity (η_a) of the uniform elastic thickness model is adjusted so that the difference in post-emplacement subsidence is minimised at the deformation centre, the non-uniformity appears in the overall deformation field as a displacement anomaly over the perimeter of the sill in which viscoelastic subsidence is greater for the non-uniform model. The anomaly is, however, by no more than the magnitude of ~15 % of the maximal syn-emplacement uplift, though η_a is necessarily modified to be ~0.2-10 times the non-uniform model viscosity (η_c). If ω_e is larger than a few times ω_s, a weak signature is no longer expected in the deformation field, and η_a is not significantly deviated from η_c. Since the signature appears so faintly in a displacement field, the InSAR data in the Kutcharo caldera for a period from 13 August 1993 to 9 June 1998 do not allow us to capture the non-uniformity. However, it can be

concluded that if ω_e beneath the caldera is comparable with or greater than the topographic caldera diameter (ω_c) as implied by the spatial variation of the geothermal gradient, the non-uniformity has no significant influence. Otherwise, if $\omega_e < \omega_c$, the non-uniformity influences the estimation of the crustal viscosity, but does not affect the overall deformation field. The elastic thickness non-uniformity can be theoretically captured in the deformation field, but in practice, its influence, particularly on estimating crustal viscosity, cannot be properly inferred without other geophysical data such as the geothermal gradient in and around the caldera.

Keywords: Geomechanics, Transient deformation, Numerical modelling, Rheology: crust and lithosphere, Calderas

1 INTRODUCTION

Mechanical heterogeneity of the crust is likely to be enhanced by magma and/or hydrothermal systems beneath volcanoes. Such enhanced heterogeneity would affect our understanding of magmatic activity in the crust when the activity is inferred from geodetically detected ground displacement through some quantitative model (e.g., Bianchi et al., 1987; De Natale et al., 1997; Troise et al., 2003; Masterlark, 2007; Currenti et al., 2008; Currenti et al., 2011; Geyer & Gottsmann, 2010; Bonaccorso et al., 2013; Hickey et al., 2016). It is, therefore, necessary to know how, and how much, each kind of heterogeneity would modify volcano deformation. We here particularly focus on elastic thickness non-uniformity in the upper crust.

The mechanical structure may be significantly perturbed by magma. The presence of magma by itself, and the rocks surrounding it into which magma may be intruded, form a zone that has rheologically less strength (e.g., Dragoni & Magnanensi, 1989; Newman et al., 2001; Segall, 2016; 2019). The thermal aspect would exert more widespread influence on the structure through heat conduction and/or advection (e.g., Del Negro et al., 2009; Gregg et al., 2013; Hickey et al., 2016). Indeed, geodetic data have revealed a low viscosity zone (LVZ) in the upper to middle crust beneath active volcanoes (e.g., Moore et al., 2017; Yamasaki & Kobayashi, 2018), where the spatial extent of the LVZ has also been found to be consistent with geophysical images (e.g., Honda et al., 2011; Hata et al., 2016; Hata et al., 2018).

The perturbation of the thermal structure by magma would also influence the depth of a brittle-ductile transition (e.g., Calmant et al., 1990; ten Brink, 1991; DeNosaquo et al., 2009; Omuralieva et al., 2012; Jiménez-Díaz et al., 2014; Castaldo et al., 2019). A recent study by Takahashi et al. (2017) compiled geothermal gradient data from boreholes in and around the Kutcharo caldera, eastern Hokkaido, Japan (Fig. 1), and reported that the gradient inside the caldera is ~2 times higher than that outside it. The 350 °C isotherm, which has usually been identified as the temperature corresponding to a brittle-ductile transition (e.g., Chen and Molnar, 1983; Scholz, 1988, 1998; Ranalli, 1995), is found at a depth of ~4 km at the shallowest inside the caldera, but at a depth of ~10 km outside it. Similarly, it has been found in other volcanoes that seismic activity occurs at shallower levels towards the volcano centre (e.g., Mori & Mckee, 1987; Ito, 1993; Bryan et al., 1999; Prejean et al., 2002).

The depth of the brittle-ductile transition has been shown to broadly correlate to the lower extent of the effective elastic thickness (EET) of the crust (e.g., Watts, 2001; Pollitz & Sacks, 2002; Watts & Burov, 2003; Yamasaki et al., 2008). The transition depth may possibly have some variations, depending also on stress state and/or lithologies of the upper crust (e.g., Tse & Rice, 1986; Sibson, 1986; Burov & Diament, 1995; Bonner et al., 2003), but it is expected to be shallower beneath volcanic areas, particularly where magmatic activity is high (e.g., Ranalli, 1995). Thus, the geothermal structure constructed by Takahashi et al. (2017) strongly implies that EET is likely to be thinned beneath the Kutcharo caldera. Nevertheless, the influence of spatial non-uniformity of EET on volcano deformation has not yet been examined in a detailed or systematic way.

A previous study by Yamasaki et al. (2018) showed that the thickness of an elastic layer plays an important role in viscoelastic deformation rate in response to magmatic emplacement. The emplacement of magma in the upper crust promotes surface uplift, but once its further inflation due to continuous magma supply stops, stress relaxation in viscoelastic substrate turns the ground surface to subsidence, whose rate is dependent on the elastic thickness. Such model behaviour was adopted in their study to analyse the crustal deformation in the Kutcharo caldera, assuming spatially uniform elastic thickness over the area. The study of Takahashi et al. (2017), therefore, requires their previous analysis to be revisited with respect to the elastic thickness non-uniformity.

This study employs a 3D finite element model to examine the effects of the lateral non-uniformity of elastic thickness on crustal viscoelastic behaviour in response to magma emplacement. A simplified elastic thickness variation is assumed, where an elastic layer, underlain by a viscoelastic layer with a spatially uniform viscosity, is thinner in the volcano centre than that in the periphery, and a sill-like body of magma is emplaced beneath the centre. The model behaviour is compared to the InSAR data in the Kutcharo caldera reported by Fujiwara et al. (2017) to confirm whether the non-uniformity is able to be captured in the data or not. For this purpose, the general model behaviour is first described to show how, and how much, the signature of elastic thickness non-uniformity appears at a particular surface point and in the overall deformation field. The vertical displacement is mainly focussed on, because the InSAR data used in this study predominantly represent the vertical component of the ground surface displacement. However, we also refer to the potential utility of the horizontal displacement component to reveal the non-uniformity. The outcome of this study has implications for the applicability of the uniform elastic thickness model and whether it is necessary to re-evaluate the crustal viscosity estimated by Yamasaki et al. (2018) with respect to the non-uniformity.

2 MODEL DESCRIPTION

A 3-D finite element model used in this study is schematically shown in Fig. 2. The response of the linear Maxwell viscoelastic crust and mantle to a sill-like magma emplacement in the upper crust is solved, using a parallelised finite element code, oregano_ve (e.g., Yamasaki & Houseman 2012; Yamasaki et al. 2018; Yamasaki & Kobayashi, 2018; Yamasaki et al., 2020). The model is composed of an elastic layer and an underlain viscoelastic layer, respectively, corresponding to the elastic upper crust and viscoelastic lower crust and mantle. The setup of the model is basically the same as that in Yamasaki et al. (2018). Spatially variable elastic thickness is, however, introduced into the model in this study, where the elastic layer is thinned beneath the centre of the volcano relative to the peripheral region by higher magmatic activity (e.g., Takahashi et al. 2017), and the magma emplacement occurs beneath the centre.

The model has a dimension of X_L = 192 km, Y_L = 192 km, and Z_L = 100 km in the *x*-, *y*-, and *z*-directions, respectively, which is large enough to avoid the boundary effect. The origin of right-handed coordinate system is located at the centre of the top surface. The *x*- and *y*-directions indicate the north- and east-wards, respectively. The *z*-coordinate increases with depth, so that positive and negative displacements in the *z*-direction mean subsidence and uplift, respectively. We solve the problem only in the domain $x \geq 0$ km, for which the boundary surfaces are constrained by the following conditions: the top surface has zero traction in any direction, and the surfaces on $x = 0$ and 96 km, $y = \pm$ 96 km, and z = 100 km have zero normal displacement and zero tangential tractions. The solutions in x < 0 km are obtained from those in x > 0 km. The effect of topography is ignored in this study, assuming that the top surface is originally flat.

The calculation domain is divided into 1,382,400 tetrahedral elements. Each element has 1 km length and 1 km height in the domain of x < 24 km, $|y|$ < 24 km, and z < 40 km. In the outer domain, however, the elements have 3 km length for x > 24 km and $|y|$ > 24 km, and 6 km height for z > 40 km. It has been confirmed in Yamasaki et al. (2018) that for the adopted element sizes the model predictions sufficiently fit the analytic solutions of Okada (1985; 1992) and Fukahata & Matsu'ura (2006).

The elastic layer thickness (h) varies, according to the horizontal distance (r) from the centre of the model, $r = (x^2 + y^2)^{1/2}$:

$$
\begin{aligned}
& h = h_i && \text{for } r \leq \omega_e/2 \\
& h = h_i + (r - \omega_e/2)(\Delta h/\delta) && \text{for } \omega_e/2 < r < \omega_e/2 + \delta \qquad (1) \\
& h = h_i + \Delta h && \text{for } r \geq \omega_e/2 + \delta
\end{aligned}
$$

where h_i and $h_i + \Delta h$ are, respectively, the elastic thicknesses in the central area and in the periphery, ω_e is a total horizontal width over which the elastic layer has a uniform thickness of h_i, δ is a distance interval over which h linearly changes by Δh. The model with $\Delta h = 0$ has a uniform elastic thickness (UET), and that with $\Delta h > 0$ non-uniform (NET). In this study, h_i is fixed to be 5 km, in keeping with Takahashi et al. (2017).

The viscoelastic layer has a spatially uniform viscosity of η_c. The constant elastic properties of the rigidity ($\mu = 3\times10^{10}$ Pa) and Poisson's ratio ($v = 0.25$) are adopted everywhere in the model. The seismological studies of Katsumata (2010) and Iwasaki et al. (2013) revealed that the crust has a thickness of 40 km beneath the Kutcharo caldera. So, a different value of the viscosity may have to be adopted as the mantle viscosity at greater depths than 40 km in the model. Since this study considers magma emplacement at depths much shallower than the mid-crust, however, the mantle viscosity has insignificant influence on the viscoelastic ground surface displacement (Yamasaki et al. 2018). Thus, the viscosity η_c effectively corresponds to the lower crustal viscosity.

Gravity is omitted in this study. Yamasaki et al. (2018) confirmed that the gravity effect caused by the vertical movement of the ground surface changes the post-emplacement viscoelastic displacement by no more than ~1 % for the optimal model that best explains the crustal deformation in the Kutcharo caldera. A significant density contrast is also expected at the Moho. However, its contrast is much smaller than that at the ground surface. In addition, the optimal model for the Kutcharo caldera predicts the vertical displacement at a depth of 40 km to be less than ~1 % of the surface uplift due to magma emplacement. Thus, the gravity effect induced by the density interface at the Moho is also negligibly small.

The geometry of magma emplacement is approximated as a horizontally elongated oblate spheroid, where a depth of the equatorial plane is d_s, the equatorial radius is $\omega_s/2$, and the thickness at the centre is s_c. The emplacement only in the elastic layer is considered, i.e., $d_s \le h_i$, and it is always centred on $x = y = 0$. For $\omega_s > \omega_e$, some or most part of the emplacement is intruded into the peripheral thickened elastic layer. For our experiments where we are exploring the general behaviour of the model, s_c is assumed to become s_{cp} instantaneously at $t = 0$, and it remains constant afterwards (see Fig. 2b). For the application to the Kutcharo caldera, s_c linearly increases with time to have $s_c = s_{cp}$ at $t = \Delta t$, and maintains s_{cp} for $t > \Delta t$ (see Fig. 2b) The emplacement is implemented into the code by Yamasaki & Houseman (2012) in terms of the split node method developed by Melosh & Raefsky (1981), where the sill opening prescribed by the difference in vertical displacement is converted into equivalent nodal force.

3 RESULTS

3.1 General model behaviour

3.1.1 Surface displacement at the centre of the model

Fig. 3 shows vertical displacement (u_z) at the centre of the modelled upper surface for NET models with $h_i = d_s = 5$ km, $\Delta h = 10$ km, $\delta = 5$ km, $\omega_s = 20$ km, and $\omega_e = 40$, 30, 20, 10, 5, and 2 km. It is noted that the subsidence caused by the viscoelastic relaxation is greater for $d_s = h_i$ than for $d_s < h_i$ (Yamasaki et al., 2018). Thus, the investigation here is based on the model in which the effect of viscoelastic relaxation on the post-emplacement surface subsidence is maximised. The time t is normalised by the Maxwell relaxation time τ (= η_c/μ). $\zeta = u_z/u_{z0}$ at the model origin is plotted in the figure, instead of u_z, where u_{z0} is an initial elastic uplift due to an instantaneous sill-like magma emplacement at $t/\tau = 0$. The dashed line indicates the normalised vertical displacement ($\zeta_u = u_{zu}/u_{z0}$) for a UET model that has a spatially uniform elastic thickness of h_i.

The surface, instantaneously uplifted by a sill-like magma emplacement at $t/\tau = 0$, continuously subsides with time. The models with $\omega_e \leq 10$ km predict ζ to be larger than ζ_u, indicating that post-emplacement subsidence is very limited, compared with that for the UET model. Since the horizontal extent of magma emplacement (ω_s) is greater than the horizontal width (ω_e) over which the elastic layer is thinned (see Fig. 2a), the emplacement-caused elastic strain is distributed more into the elastic layer where any stress relaxation is not allowed to occur. Thus, the available post-emplacement subsidence due to viscoelastic relaxation is smaller than that for the UET model.

The models with $\omega_e \geq 20$ km, on the other hand, predict ζ to be smaller than ζ_u, indicating greater post-emplacement subsidence due to viscoelastic relaxation than that for the UET model. We have confirmed that for these cases, ζ in the final equilibrium state is not significantly different from ζ_u. The model with $\omega_e = 20$ km, however, predicts ζ in the equilibrium state to be slightly larger than that for the UET model, because the magma emplacement distributes some more initial strain into the elastic layer. Nevertheless, in general, the rate of subsidence early in the post-emplacement period is smaller for greater ω_e. Such model behaviour is consistent with previous studies where the viscoelastic surface displacement rate is greater for a thicker elastic layer (e.g., Fukahata and Matsu’ura, 2018; Yamasaki et al., 2018).

Fig. 4 shows ζ as a function of time for four different values of ω_s, where the difference of ζ from ζ_u, i.e., $\Delta\zeta_u = \zeta - \zeta_u$, is plotted. The other model parameters are the same as those in Fig. 3. The horizontal dashed line at $\Delta\zeta_u = 0$ indicates the behaviour of the UET model. $\Delta\zeta_u$ below the line indicates that NET models predict greater post-emplacement subsidence, and that above the line smaller subsidence. The model behaviour for a given ω_s depends on ω_e in the similar way shown in Fig. 3.

The magnitude of the deviation is dependent on the ratio of ω_e to ω_s. For the models where $\Delta\zeta_u$ is predicted to be negative, the deviation becomes smaller for smaller ratios of ω_s/ω_e. For models where $\Delta\zeta_u$ is predicted to be positive, however, the behaviour becomes slightly complicated. The models with ω_e = 2 km and ω_s = 8 km show the greatest deviation. For smaller ω_s (= 4 km), but keeping ω_e at 2 km, the deviation from the UET model is less significant. This is because a lesser amount of the initial elastic strain is distributed into the thicker elastic layer by magma emplacement. For greater ω_s (= 20 km), on the other hand, a greater amount of the initial elastic strain is distributed into the viscoelastic layer, resulting in less deviation from the UET model.

The model with ω_s = 40 km predicts $\Delta\zeta_u$ to be negative early in the post-emplacement period, but positive later in the period as apparent in the general behaviour for $\omega_s > \omega_e$. ω_s = 40 km is such a large horizontal extent of magma emplacement that the initial elastic strain distributed into the underlain viscoelastic layer is significantly more than that for smaller ω_s. This causes greater subsidence early in the post-emplacement period. However, later in the period, the lack of stress relaxation in the elastic layer becomes a dominant effect for characterising the model behaviour.

We have further explored the model behaviour for other model parameters, including d_s, Δh, and δ, in Appendix A. It has been confirmed that the model behaviour depends on the non-uniformity in the same way shown above; the lack of stress relaxation in the elastic layer results in smaller post-emplacement subsidence, and the post-emplacement viscoelastic subsidence is enhanced by the presence of a thickened elastic layer in the peripheral region unless ω_e is a few times greater than ω_s

3.1.2 Overall surface displacement field

We have described above that if the ground displacement only at the deformation centre is considered, ζ is smaller or greater than ζ_u, depending on the model parameters that characterise the non-uniformity of elastic thickness. Here we describe the influence of the non-uniformity on overall vertical surface displacement field. The deviation of ζ from ζ_u is calculated at any surface points, for which the difference at the deformation centre is minimised by applying an apparent viscosity η_a to the UET model. ζ_a is here defined as a vertical displacement normalised by an initial elastic uplift for a UET model with $\eta = \eta_a$.

Fig. 5 shows temporal ζ_a (solid blue) at the centre of the modelled upper surface, in comparison with ζ (solid red) and ζ_u (dashed blue). ω_s, Δh, and δ are adopted to be 20 km, 10 km, and 5 km, respectively. η_a is dependent on a time interval (t_{int}) over which the deviation between ζ and ζ_u is minimised, and on the elastic thickness non-uniformity. For the models with ω_e = 20 km, ζ_a mimics ζ well. ζ_u is predicted to be greater than ζ, so that

η_a/η_c is required to be less than 1. It is also found that η_a/η_c is smaller for greater t_{int} (see Fig. 5a-d).

For the models with ω_e = 10 km, on the other hand, ζ is predicted to be larger than ζ_u, which requires η_a/η_c to be greater than 1. It is also found for this case of ω_e that η_a/η_c is larger for larger values of t_{int}. In addition, for $t_{int} \geq 5\tau$, a significant deviation of ζ_a from ζ is perceptible, where ζ is slightly smaller and greater than ζ_a earlier and later in the time interval.

Fig. 6 summarises the ratio η_a/η_c, with which the difference between ζ_u and ζ is minimised at the deformation centre, as a function of ω_s/ω_e. η_a/η_c varies with ω_s/ω_e in a complex way, where the available upper and lower values are greater for greater Δh and/or t_{int}. In general, however, the model behaviour described above is clearly reflected in the distribution of η_a/η_c. When $\omega_s \leq \omega_e$, i.e., $\omega_s/\omega_e \leq 1$, the post-emplacement subsidence for the NET model is greater than that for the UET model, which causes η_a/η_c to be less than 1. When ω_e is a few times greater than ω_s, however, the deviation of η_a/η_c from 1 is insignificant. On the other hand, since the NET model predicts less post-emplacement subsidence for a small ω_e relative to ω_s (i.e., $\omega_s/\omega_e > 1$), η_a/η_c is greater than 1, where η_a/η_c increases with ω_s/ω_e. However, η_a/η_c starts to decrease for greater ω_s/ω_e, the behaviour of which is dependent on ω_e. Indeed, the numerical experiment has shown that the NET model with a large value of ω_s (= 40 km) predicts greater subsidence early in the post-emplacement period (see Fig. 4d). It seems that the model behaviour for such a large ω_s is not controlled only by the ratio ω_s/ω_e, but also by the characteristic of the elastic thickness non-uniformity itself. This is, however, not the case for the Kutcharo caldera where ω_s is required to be 4 km (Yamasaki et al., 2018). Thus, we do not further examine such an extreme case in this study.

Fig. 7 shows spatial distribution of $\Delta\zeta_a = \zeta - \zeta_a$ at $t = 5\tau$, for which η_a is determined for a time interval of $t_{int} = 5\tau$. $h_i = d_s = 5$ km, $\Delta h = 10$ km, and $\delta = 5$ km are adopted. Some significant difference appears at the deformation centre in some models even though η_a is obtained so that $\Delta\zeta_a$ is minimised at the centre. This is because the minimization is obtained from the comparison made over the whole time interval $t_{int} = 5\tau$, not minimised only at $t = 5\tau$; for example, the NET model with $\omega_s > \omega_e$ predicts greater and smaller subsidence than the UET model with $\eta = \eta_a$ earlier and later in the period, respectively (see Fig. 5).

The models with $\omega_s = 8$ km and $\omega_e \leq 20$ km (Fig. 7a-c) predict a region where $\Delta\zeta_a$ is negative (i.e., the post-emplacement subsidence is greater for the NET model), which appears concentrically with respect to the deformation centre. The maximum negative anomaly is found at r (the distance from the centre of the model) = ~6-7 km, a few km further than $\omega_s/2$. The available magnitude of the negative $\Delta\zeta_a$ is greater for smaller ω_e, but it is no more than ~0.15; the magnitude is at most only ~15 % of the initial elastic uplift due to instantaneous magma emplacement. In contrast, the model with $\omega_s = 8$ km and $\omega_e = 40$ km predicts no significant $\Delta\zeta_a$ at any distance from the deformation centre (Fig. 7d).

Similar behaviour is found for the models with $\omega_s = 20$ km (Fig. 7e-g). The negative anomaly $\Delta\zeta_a$ peaks at r = ~10-11 km, approximately above the perimeter of the sill. The available magnitude of the anomaly is, however, greater for greater ω_e when ω_e is less than 20 km. The magnitude of the negative deviation is no greater than ~0.15, which is the same as that for $\omega_s = 8$ km. $\Delta\zeta_a$ is insignificant when ω_e is 40 km (Fig. 7h).

The dependence of $\Delta\zeta_a$ on the other model parameters, including t_{int} and Δh, has been explored in Appendix B, which shows the same general model behaviour that a region in which $\Delta\zeta_a$ is negative appears; the peak is found over the perimeter of the deformation source. It has also been found that the available magnitude of the negative $\Delta\zeta_a$ is greater for greater t_{int} and/or greater Δh, but it is no more than ~15 % of the initial elastic uplift due to instantaneous magma emplacement.

We here describe the horizontal displacement component. Fig. 8 shows spatial distribution of $\Delta\upsilon_a = \upsilon - \upsilon_a$ at $t = 5\tau$, where υ is the NET model displacement in y-direction (u_y) normalised by the absolute value of u_{z0}, i.e., $\upsilon = u_y/|u_{z0}|$, and υ_a is the normalised displacement for the UET model with $\eta = \eta_a$. The model parameters are the same as those in Fig. 7. We use $|u_{z0}|$, instead of u_{y0} at some surface point, to get the normalised displacement. This is because we here aim to know the potential contribution of the horizontal component to the LOS (line of sight) displacement which will be used for the application to the Kutcharo caldera. η_a is determined so that $\Delta\zeta_a$ is minimised at the centre for a time interval of $t_{int} = 5\tau$. The sign of $\Delta\upsilon_a$ is reversed with respect to $y = 0$, because u_y is negative for $y < 0$. For $y > 0$, the positive and negative values, respectively, mean that the NET model displacement is larger and smaller than the UET model, but for $y < 0$ the sense is opposite.

$\Delta\upsilon_a$ is zero on $y = 0$, but it varies with y in a more complex way than $\Delta\zeta_a$. In the domain $y > 0$, the positive $\Delta\upsilon_a$ peaks at y = ~3-4 km and ~7-8 km for ω_s = 8 and 20 km, respectively. $\Delta\upsilon_a$ is negative at further distance, and its peak is found at y = ~10 km and ~15 km for ω_s = 8 and 20 km, respectively. The magnitude of $\Delta\upsilon_a$ is, however, no more than ~0.05, i.e., ~5 % of the initial elastic uplift at the centre. Thus, the non-uniform elastic thicknesses cause only small changes to the horizontal component of surface deformation compared to the vertical component.

3.2. Application to the Kutcharo caldera

We here apply the viscoelastic model behaviour to analyse the crustal deformation observed in the Kutcharo caldera. InSAR data in and around the Kutcharo caldera showed that the ground surface was uplifted at least since 13 August 1993, with a deformation centre near the Atosanupuri volcano, but suddenly began to subside around early 1995 (Fujiwara et al., 2017). Fujiwara et al. (2017) explained the uplift by magma emplacement, and the subsequent subsidence by magma drain back. Yamasaki et al. (2018), on the other hand, proposed viscoelastic relaxation for the post-emplacement subsidence. Here we analyse the InSAR data in terms of viscoelastic relaxation to see whether or not the signature of elastic thickness non-uniformity can be detected.

The viscoelastic model behaviour described in the previous section assumed an instantaneous magma emplacement. We here first analyse the model behaviour with finite emplacement period, for which LOS displacement, particularly for the case of the Kutcharo caldera, is calculated using the line-of-sight vector from the Japanese Earth Resources Satellite (JERS)-1 to points on the ground surface. For the JERS-1 orbit with an incidence angle of ~39°, the LOS displacement is calculated by $0.11u_x - 0.62u_y + 0.78u_z$, where u_x, u_y, and u_z are the northward, eastward and vertical ground surface displacements, respectively; note that u_z is negative for the uplift in this study. The northward component contributes much less than the other two components. The percentages of the eastward and vertical components are comparable, although the magnitude of the former is smaller.

All the model parameters, except elastic thickness non-uniformity, follow the outcome of Yamasaki et al. (2018). The magma emplacement period Δt is 626 days, from 13 August 1993 to 1 May 1995; see Yamasaki et al. (2018) for the details. The emplacement depth d_s is 4.56 km, the emplaced horizontal width ω_s is 4 km, and spatially-uniform viscosity η_k is

4×10^{17} Pa s. h_i = 5 km and Δh = 5 km are adopted for the NET model, as suggested by Takahashi et al. (2017).

η_k is adopted for the viscosity η_c of the NET model, i.e., $\eta_c = \eta_k$. In fact, the estimation of η_k was based on the uniform elastic thickness model in Yamasaki et al. (2018). However, the important point here is to assess the difference between the NET and UET models. We do not know the actual NET model viscosity to best explain the InSAR data, but what viscosity is necessary can be inferred from η_a adjusted so that the difference is minimised at the deformation centre.

Fig. 9 shows the difference in LOS displacement change between the NET model with $\eta = \eta_k$ and UET model with $\eta = \eta_a$ in four different stages: (I) 13 August 1993 - 21 April 1995, (II) 21 April 1995 - 07 April 1996, (III) 07 April 1996 - 25 March 1997, and (IV) 25 March 1997 - 09 June 1998. η_a is determined so that the difference in post-emplacement viscoelastic subsidence is minimised at the deformation centre for a period from 1 May 1995 to 9 June 1998, i.e., t_{int} = 1135 days (Yamasaki et al., 2018). The stage I represents the syn-emplacement period, and the subsequent three stages (II – IV) of the post-emplacement period. Since LOS displacement is the change in distance from a satellite, ground surface uplift and subsidence are referred as negative and positive LOS displacement change, respectively. The difference at 1 May 1995 is zero at the centre of the deformation field, because a thickness of sill-like magma emplacement s_c is given so that the predictions are equal to the observation at the deformation centre at the end of the syn-emplacement period. η_a is required to be ~208 %, ~74 %, ~92 %, and ~100 % of η_k (= η_c) for ω_e = 2, 10, 20, and 40 km, respectively.

The differences between the NET and UET models appear almost concentrically with respect to the centre of the LOS displacement field. The deformation centre is shifted only by ~800 m from the centre of the deformation source. This indicates that the LOS displacement predominantly represents the vertical ground surface displacement, and the effect of the horizontal displacement is relatively minor. The displacement anomaly at the deformation centre may possibly be caused by the fact that η_a is determined by minimising the difference between the NET and UET models over a finite time period of t_{int} = 1135 days. As described above (see the section 3.1.2), the signature of elastic thickness non-uniformity would more likely correspond to the anomaly at R (the distance from the LOS displacement centre) ~ $\omega_s/2$ or a few km further away. Indeed, the NET model predicts greater subsidence than the UET model, except the NET model with ω_e = 40 km. The difference for ω_e = 2 km is up to ~1.5 cm early in the post-emplacement period; < ~8 % of the maximum LOS displacement magnitude (~19.5 cm) in the syn-emplacement period, but it is limited to be less than ~0.5 cm later in the period. For the models with greater ω_e, on the other hand, the difference is ~0.5 cm or smaller at any stage in the period.

Fig. 10 shows the observed and predicted LOS displacement change fields, and the residuals, during the four different stages. The UET model with η_a (= η_k) = 4 × 10^{17} Pa s is adopted for the predictions as this value of η_a was constrained by Yamasaki et al. (2018) so that the post-emplacement subsidence at the deformation centre is best explained by the UET model. In the stage II, a region where a greater subsidence is observed appears only in the distance range from the deformation centre greater than 5 km. However, the magnitude of the anomaly is a few times to a few tens of times larger in the observation than in the predictions, depending on the values of ω_e (see Fig. 9). In the stages of I, III, and IV, on the other hand, a region where the observation shows greater subsidence than the UET model prediction appears at R < ~5 km. The magnitude of the deviation is again much greater than that predicted in Fig. 9. This indicates that a lot of noise and/or some local phenomena, which surpass the signature of elastic thickness non-uniformity, are convolved in the InSAR data. Thus, the InSAR data for the period from 13 August 1993 to 09 June 1998 are not readily explained by elastic layer thickness non-uniformity.

Alternatively, using the NET models with various ω_e and Δh, we evaluate the fitting between the predictions and observation in terms of root mean square misfit (ε) in each of the four different stages:

$$\varepsilon = \sqrt{\frac{1}{N}\sum_{j=1}^{N}\left(\Delta u_{Lo} - \Delta u_{Lp}\right)^2} \tag{2}$$

where Δu_{Lo} and Δu_{Lp} are the observed and predicted LOS displacement changes, respectively, and N is the number of the surface points at which Δu_{Lp} is compared with Δu_{Lo}; see Yamasaki & Kobayashi (2018) for the values of N in each time period. Table 1 summarises ε, the averaged ε of the four stages: $\varepsilon = (\varepsilon_{\mathrm{I}} + \varepsilon_{\mathrm{II}} + \varepsilon_{\mathrm{III}} + \varepsilon_{\mathrm{IV}})/4$, for which the viscosity η_c of the NET model is modified from $\eta_k = 4\times10^{17}$ Pa s so that the observed post-emplacement displacement at the deformation centre is best explained. ω_s and δ are fixed to be 4 km and 5 km, respectively. Takahashi et al. (2017) suggests Δh to be ~5 km for the case of the Kutcharo caldera, but here we consider greater Δh (= 10 and 15 km) too.

All the models shown in Table 1 predict almost the same values of ε, ~2.2-2.5 cm. It is still perceptible that ε is smaller for greater ω_e, but the difference is no more than ~0.3 cm. However, η_c is required to be significantly modified from $\eta_k = 4\times10^{17}$ Pa s, depending on ω_e. Ratio η_c/η_k is smaller than 1 when ω_e is 2 km, smaller than ω_s (= 4 km), where η_c/η_k is 0.47, 0.21 and 0.13 for Δh = 5, 10 and 15 km, respectively. For ω_e = 6 and 10 km, the ratio becomes greater than 1, because the effect of thickened elastic layer in the periphery appears on post-emplacement viscoelastic subsidence rate. For $\omega_e \geq 20$ km, however, η_c is insignificantly different from η_k.

4 DISCUSSION

In this study, we have examined the influence of an elastic thickness that is effectively thinned in the volcano centre, compared with that in the peripheral region, on viscoelastic deformation in response to a sill-like magma emplacement beneath the centre. The elastic thickness non-uniformity has two different effects on viscoelastic surface displacement. One effect appears when the horizontal width of the magma emplacement (ω_s) is greater than that of the thinner elastic thickness area (ω_e), where emplacement-induced elastic strain is distributed more into the relatively thicker elastic layer. This results in post-emplacement viscoelastic displacement being very limited, because any stress relaxation does not occur in the elastic layer. Another effect appears when ω_s is comparable or smaller than ω_e. For this case, the viscoelastic deformation rate is higher than that for models without thickened elastic layer in the periphery, and the difference between NET and UET models becomes smaller for smaller ratio of ω_s/ω_e. Each of these effects appears with different magnitude at different timing, depending on the configuration of the non-uniformity.

The signature of the elastic thickness non-uniformity, if it is inferred from ground displacement at the deformation centre, appears in such a way that the relaxation-caused ground displacement is greater or smaller than that predicted by models with uniform elastic thickness. In practice, however, such a difference in rate of relaxation-caused ground displacement would be explained by applying lower or higher crustal viscosity.

Thus, the non-uniformity should not be discussed only in relation to the displacement at a particular surface point.

It has been shown in this study that the signature of the non-uniformity can be captured in the overall deformation field. If the difference in vertical displacement (u_z) between the NET model with $\eta = \eta_c$ and UET model with $\eta = \eta_a$ is minimised at the deformation centre by adjusting the value of η_a, a region in which Δu_z is negative appears over the perimeter of the deformation source (i.e., the NET model predicts greater subsidence than the UET model). However, the magnitude of the negative deviation is only up to ~15 % of the initial elastic uplift due to instantaneous magma emplacement, although η_a is possibly required to be significantly modified from η_c.

The available deviation is expected to be so weak that the elastic thickness non-uniformity is detectable only by precise geodetic measurements. The noise and/or some local phenomena with the magnitudes more than a few cm may prevent us to capture the non-uniformity in deformation field. Indeed, the application to the Kutcharo caldera has found that the influence of elastic thickness non-uniformity on the fitting to LOS displacement field is so minor that the LOS displacement misfit changes by no more than ~0.3 cm for any configuration of the non-uniformity. However, if ω_e is less than a few times ω_s, the effective crustal viscosity is required to be modified from the previous estimate of Yamasaki et al. (2018), and its magnitude depends on the ratio of ω_e to ω_s and on how much the elastic crust is thickened in the peripheral region of the volcano. If, on the other hand, ω_e is greater than a few times ω_s, significant modification of the viscosity is not necessary. The survey of the geothermal gradient in and around the Kutcharo caldera showed that the depth of the 350 °C isotherm is ~4-6 km in the caldera, and a significantly thickened elastic layer is found only outside the caldera (Takahashi et al., 2017), i.e., ω_e >

~20 km (see Fig. 1) compared with ω_s = ~4 km. Thus, there seems no need to re-evaluate the crustal viscosity in a significant way.

The elastic thickness non-uniformity adopted in this study may be oversimplified. The non-uniformity may be significantly deviated from axial symmetry. However, the signature of a negative deviation in vertical displacement should appear in the same way, though it is expected not to have a symmetric distribution relative to the deformation centre. The same argument would apply in the case of the elastic thickness gradually increasing towards the peripheral region of the volcano. The gradient of the thickness change modifies the effective horizontal width over which the elastic layer is thinned uniformly, by which the available signature may be attenuated; the deviation from the UET model behaviour changes more gradually as the distance from the deformation centre increases, and the modification of the apparent viscosity would possibly be less. In any case, however, we cannot expect the anomaly magnitude to be more than ~15 % of the maximal syn-emplacement uplift.

Since the NET model has very limited potential to significantly improve the fitting to the data in the Kutcharo caldera, the residual misfit of the UET model to the observation requires other deformation mechanism. For this purpose, a spatially averaged vertical displacement as a function of distance from the centre of the uplift may provide the clue of the most likely mechanism to better explain the InSAR data. The topographic effect may also improve the fitting. Trasatti et al. (2003) showed that the topography has only minor effect on the surface displacement field, but it is still detectable. So, the misfits (ε) of a few cm may possibly be diminished by taking it into account.

This study also provides general implications for other volcanoes. If no knowledge about the geothermal structure such as the study of Takahashi et al. (2017) is available, the signature of the non-uniformity only relies on geodetic data. The adoption of the method shown in this study for the data may enable the deviation from the UET model behaviour to be estimated. In most cases, however, where the signature of the non-uniformity is obscured by unavoidable noise and/or local deformation, any non-uniformity would provide a similar degree of misfit to the data. This in turn indicates that the elastic thickness non-uniformity does not significantly influence the fitting to the geodetic data. So, the adoption of a uniform elastic thickness model would be an adequate approximation. However, we still need to consider that the uncertainty of crustal viscosity due to the non-uniformity can be ~0.2-10 times the actual one (see Fig. 6 and Table 1). Thus, if the viscosity is to be constrained as precisely as possible, undertaking a survey of the geothermal structure in and around the volcano is required.

The ascent and emplacement of magma in the crust is principally controlled by the rheological layering, in which optimal magma emplacement occurs around the depth of the brittle-ductile transition, roughly corresponding to the bottom of the elastic layer (e.g., Watts, 2001; Watts & Burov, 2003; Yamasaki et al., 2008), and develops further inflation there (e.g., Rubin, 1993; Parsons et al., 1992; Hogan & Gilbert, 1995; Rubin, 1995; Watanabe et al., 1999; Burov et al., 2003). In this study, for the models with $\omega_s > \omega_e$, the edge or most part of the magma emplacement is intruded into the peripheral thickened elastic layer. However, the dynamic behaviour of magma controlled by rheological layering may effectively limit its emplacement and inflation only within the central area of volcano beneath which the elastic layer is thinner, unless magma ascends beneath the peripheral region. If that argument applies, the reduction of post-emplacement subsidence due to elastic thickness non-uniformity may not occur in a significant way.

This study has particularly considered the role of elastic thickness non-uniformity as a mechanical heterogeneity in active volcanic regions. Many other kinds of mechanical heterogeneity would be expected to be present within various spatial scales. Yamasaki & Kobayashi (2018), however, showed that if the spatial dimension of viscosity heterogeneity is much greater than that of a deformation source, the effect of the heterogeneity is negligible. Our present study has provided a similar finding for elastic thickness non-uniformity, where only a heterogeneity with spatial dimension that is smaller than a few times the magma emplacement width would play an important role in volcano deformation. Heterogeneity on a much smaller scale could also possibly be present, but such fine-scale considerations are not the objective of this study. Such small-scale heterogeneities may be rather random; their unknown origins mean that their effect on deformation at the crustal-scale is difficult to assess in a systematic way. Moreover, the effect may simply disappear in a bulk rheological property.

5 CONCLUSIONS

In this study, we have employed a 3-D linear Maxwell viscoelastic model to examine how, and how much, elastic thickness non-uniformity influences post-emplacement viscoelastic surface deformation. This was examined for a scenario in which an elastic layer in the volcano centre is uniformly thinned to be h_i over a horizontal width of ω_e, compared with $h_i + \Delta h$ in the peripheral region of the volcano, and a sill-like magma emplacement, whose horizontal width is ω_s, occurs beneath the centre. The influence of the non-uniformity on the deformation field was evaluated in the comparison of the NET (non-uniform elastic thickness) model behaviour with that of the UET (uniform elastic thickness) model with an elastic thickness of h_i.

We have found that the elastic thickness non-uniformity modifies the vertical ground surface displacement, depending on whether or not ω_s is greater than ω_e. The non-uniformity with $\omega_s \leq \omega_e <$ a few times ω_s enhances post-emplacement viscoelastic subsidence at the deformation centre. The subsidence at the deformation centre for the non-uniformity with $\omega_e < \omega_s$ is, on the other hand, significantly diminished. Such NET model behaviours are, however, inappropriate to regard as the signature of non-uniformity, because the difference in viscoelastic subsidence rate can also be explained by adopting a different crustal viscosity; we cannot distinguish the effects of the elastic thickness non-uniformity and crustal viscosity

We have also found that the signature of the elastic thickness non-uniformity can be captured in the spatial variation of the deformation field. The difference in the vertical ground surface displacement field of the NET model from that of the UET model, for which the difference at the deformation centre is minimised by adopting an apparent viscosity η_a for the UET model, reveals the non-uniformity as a displacement anomaly over the perimeter of the deformation source, in which post-emplacement viscoelastic subsidence is greater for the NET model. The magnitude of the deviated subsidence is no more than ~15 % of the maximal syn-emplacement uplift at the deformation centre, but η_a is required to be modified significantly from the NET model viscosity. If ω_e is greater than a few times ω_s, however, even any weak signature cannot be expected, and η_a is not significantly modified.

The InSAR data for the Kutcharo caldera (Fujiwara et al., 2017) for the period between 13 August 1993 and 9 June 1998 have been analysed on the basis of the general model behaviour described in this study. The adoption of the UET model with $\eta = \eta_a$ for the InSAR data has brought out no clear signature of elastic thickness non-uniformity, where η_a =

$4{\times}10^{17}$ Pa s was constrained in Yamasaki et al. (2018) so that the UET model best explains the observed post-emplacement LOS displacement change at the deformation centre. Models with various non-uniformity have also been adopted, but no significant difference in the fitting to the displacement field has been found. Nevertheless, the viscosity η_c of the NET model is necessarily modified at most by several tens % of the estimation of Yamasaki et al. (2018). However, the study of Takahashi et al. (2017) on the spatial variation of the geothermal gradient implies that the non-uniformity beneath the Kutcharo caldera has a spatial scale significantly greater than that of the deformation source, i.e., ω_e is larger than a few times ω_s. Thus, it can be concluded that significant modification of the crustal viscosity is not required.

This study has shown that the optimal viscoelastic model with spatially uniform elastic thickness can be found to sufficiently explain geodetic data at volcanoes. However, an ambiguity between the viscosity and/or elastic thickness non-uniformity remains. Not only geodetic data but also other geophysical data are, therefore, required to constrain these mechanical properties in a more robust way. Since magmatic activity, particularly its dynamic behaviour, is controlled by the mechanical structure of the crust, only an interdisciplinary study that integrates different kinds of data set can reach a better understanding of volcanic unrest.

ACKNOWLEDGEMENTS

The InSAR dataset in and around the Kutcharo caldera was kindly provided by Satoshi Fujiwara. We thank Chris Conway for discussion and suggestions. We are grateful to Gregory Houseman and an anonymous reviewer for very careful and constructive reviews. The calculations in this study were conducted on the computer system of the Earthquake and Volcano Information Center of the Earthquake Research Institute (EIC), The University of Tokyo. Generic Mapping Tools (GMT; Wessel et al., 2013) was used to produce the figures. COMET is the NERC Centre for the Observation and Modelling of Earthquakes, Volcanoes and Tectonics, a partnership between UK Universities and the British Geological Survey.

REFERENCES

Bianchi, R., Coradini, A., Federico, C., Giberti, G., Lanciano, P., PozzI, J.P., Sartoris, G. & Scandome, R., 1987. Modeling of surface deformation in volcanic areas: The 1970-1972 and 1982-1984 crises of Campi Flegrei, Italy, *J. Geophys. Res.*, **92**, 14,139-14,150.

Bonaccorso, A., Currenti, G. & Del Negro, C., 2013. Interaction of volcano-tectonic fault with magma storage, intrusion and flank instability: A thirty years study at Mt. Etna volcano, *J. Vocanol. Geotherm. Res.*, **251**, 127-136.

Bonner, J.L., Blackwell, D.D. & Herrin, E.T., 2003. Thermal Constraints on Earthquake Depths in California, *Bull. Seism. Soc. Am.*, **93**, 2333-2354.

Bryan, C.J., Sherburn, S., Bibby, H.M., Bannister, S.C. & Hurst, A.W., 1999. Shallow seismicity of the central Taupo Volcanic Zone, New Zealand: Its distribution and nature, New Zeal. J. Geol. Geop., **42:4**, 533-542.

Burov, E.B. & Diament, M., 1995. The effective elastic thickness (Te) of continental lithosphere: what does it mean?, *J. Geophys. Res.*, **100**, 3905-3927.

Burov, E, Jaupart, C. & Guillou-Frottier, L., 2003. Ascent and emplacement of buoyant magma bodies in brittle-ductile upper crust, *J. Geophys. Res.*, **108**, 2177, doi:10.1029/2002JB001904.

Calmant, S., Francheteau, J. & Cazenave, A., 1990. Elastic layer thickening with age of the oceanic lithosphere: a tool for prediction of the age of volcanoes or oceanic crust, *Geophys. J. Int.*, **100**, 59-67.

Castaldo, R., D'Auria, L., Pepe, S., Solaro, G., De Novellis, V. & Tizzani, P., 2019. The impact of crustal rheology on natural seismicity: Campi Flegrei caldera case study, *Geosci. Front.*, **10**, 453-466.

Chen, P.-J. & Molnar, P., 1983. Focal depths of intracontinental and intraplate earthquakes and their implications for the thermal and mechanical properties of the lithosphere, *J. Geophys. Res.*, **88**, 4183-4214.

Currenti, G., Del Negro, C., Ganci, G. & Scandura, D., 2008. 3D numerical deformation model of the intrusive event forerunning the 2001 Etna eruption, *Phys. Earth Planet. Inter.*, **168**, 88-96.

Currenti, G., Napoli, R. & Del Negro, C., 2011. Toward a realistic deformation model of the 2008 magmatic intrusion at Etna from combined DInSAR and GPS observations, *Earth Planet. Sci. Lett.*, **312**, 22-27.

Del Negro, C., Currenti, G. & Scandura, D., 2009. Temperature-dependent viscoelastic modeling of ground deformation: Application to Etna volcano during the 1993-1997 inflation period, *Phys. Earth Planet. Inter.*, **172**, 299-309.

De Natale, G., Petrazzuoli, S.M. & Pingue, F., 1997. The effect of collapse structures on ground deformations in calderas, *Geophys. Res. Lett.*, **24**, 1555-1558.

DeNosaquo, K.R., Smith, R.B. & Lowry, A.R., 2009. Density and lithospheric strength models of the Yellowstone–Snake River Plain volcanic system from gravity and heat flow data, *J. Volcanol. Geotherm. Res.*, **188** 108–127.

Dragoni, M. & Magnanensi, C., 1989. Displacement and stress produced by a pressurized, spherical magma chamber, surrounded by a viscoelastic shell, *Phys. Earth Planet. Inter.*, **56**, 316-328.

Farr, T. G., Rosen, P.A., Caro, E., Crippen, R., Duren, R., Hensley, S., Kobrick, M., Paller,, M., Rodriguez, E., Roth, L., Seal, D., Shaffer, S., Shimada, J., Umland, J., Werner, M., Oskin, M., Burbank, D. & Alsdorf, D., 2007. The Shuttle Radar Topography Mission, *Rev. Geophys.*, **45**, RG2004, doi:10.1029/2005RG000183.

Fujiwara, S., Murakami, M., Nishimura, T., Tobita, M., Yarai, H. & Kobayashi, T., 2017. Volcanic deformation of Atosanupuri volcanic complex in the Kussharo caldera, Japan, from 1993 to 2016 revealed by JERS-1, ALOS, and ALOS-2 radar interferometry, *Earth, Planets and Space*, **69**, 78, doi: 10.1186/s40623-017-0662-y.

Fukahata, Y. & Matsu'ura, M., 2006. Quasi-static internal deformation due to a dislocation source in a multilayered elastic/viscoelastic half-space and an equivalence theorem, *Geophys. J. Int.*, **166**, 418-434.

Fukahata, Y. & Matsu’ura, M., 2018. Characteristics of viscoelastic crustal deformation following a megathrust earthquake: Discrepancy between the apparent and intrinsic relaxation time constants, *Pure Appl. Geophys.*, **175**, 549-558.

Geyer, A. & Gottsmann, J., 2010. The influence of mechanical stiffness on caldera deformation and implications for the 1971-1984 Rabaul uplift (Papua New Guinea), *Tectonophysics*, **483**, 399-412.

Gregg, P.M., de Silva, S.L. & Grosfils, E.B., 2013. Thermomechanics of shallow magma chamber pressurization: Implications for the assessment of ground deformation data at active volcanoes, *Earth Planet. Sci. Lett.*, **384**, 100-108.

Hata, M., Takakura, S., Matsushima, N., Hashimoto, T. & Utsugi, M., 2016. Crustal magma pathway beneath Aso caldera inferred from three-dimensional electrical resistivity structure, *Geophys. Res. Lett.*, **43**, 10,720-10,727.

Hata, M., Uyeshima, M., Tanaka, Y., Hashimoto, T., Oshiman, N. & Yoshimura, R., 2018. Three-dimensional electrical resistivity distribution beneath the Beppu–Shimabara graben with a focus on Aso Caldera, southwest Japan subduction zone, *J. Geophys. Res. Solid Earth*, **123**, 6397–6410.

Hickey, J., Gottsmann, J., Nakamichi, H. & Iguchi, M., 2016. Thermomechanical controls on magma supply and volcanic deformation: application to Aira caldera, Japan, *Sci. Rep.*, **6**, 32691, doi: 10.1038/srep32691.

Hogan, J.P. & Gilbert, M.C., 1995. The A-type Mount Scott Granite sheet: Importance of crustal magma traps, *J. Geophys. Res.*, **100**, 15,779-15,792.

Honda, R., Yamaya, Y., Ichihara, H., Hase, H., Mogi, T., Yamashita, H., Ohyama, T., Uyeshima, M. & Nakagawa, M., 2011. Magnetotelluric investigation around the Kutcharo caldera region, *Geophys. Bull. Hokkaido Univ., Sapporo, Japan*, **74**, March, 45-55 (in Japanese with English abstract).

Ito, K., 1993. Cutoff depth of seismicity and large earthquakes near active volcanoes in Japan, *Tectonophysics*, **217**, 11-21.

Iwasaki, T., Levin, V., Nikulin, A. & Iidaka, T., 2013. Constraints on the Moho in Japan and Kamchatka, *Tectonophysics*, **609**, 184-201.

Jiménez-Díaz, A., Ruiz, J., Pérez-Gussinyé, M., Kirby, J.F., Álvarez-Gómez, J.A., Tejero, R. & Capote, R., 2014. Spatial variations of effective elastic thickness of the lithosphere in Central America and surrounding regions, *Earth Planet. Sci. Lett.*, **391**, 55-66.

Katsumata, A., 2010. Depth of the Moho discontinuity beneath the Japanese islands estimated by traveltime analysis, *Geophys. Res. Lett.* **115**, B04303, https://doi.org/10.1029/2008JB005864.

Masterlark, T., 2007. Magma intrusion and deformation predictions: Sensitivities to the Mogi assumptions, *J. Geophys. Res.*, **112**, B06419, doi:10.1029/2006JB004860.

Melosh, H.J. & Raefsky, A., 1981. A simple and efficient method for introducing faults into finite element computations, *Bull. Seism. Soc. Am.*, **71**, 1391-1400.

Moore, J.D.P., Yu, H., Tang, C.-H., Wang, T., Barbot, S., Peng, D., Masuti, S., Dauwels, J., Hsu, Y.-J., Lambert, V., Nanjundiah, P., Wei, S., Lindsey, E., Feng, L. & Shibazaki, B., 2017. Imaging the distribution of transient viscosity after the 2016 Mw 7.1 Kumamoto earthquake, *Science*, **356**, 163–167.

Mori, J. & McKee, C., 1987. Outward-dipping ring-fault structure at Rabaul Caldera as shown by earthquake locations, *Science*, **235**, 193-195.

Newman, A.V., Dixon, T.H., Ofoegbu, G.I. & Dixon, J.E., 2001. Geodetic and seismic constraints on recent activity at Long Valley Caldera, California: evidence for viscoelastic rheology, *J. Volcanol. Geotherm. Res.*, **105**, 183-206.

Okada, Y., 1985. Surface deformation due to shear and tensile faults in a half-space, *Bull. Seismol. Soc. Am.*, **75**, 1135–1154.

Okada, Y., 1992. Internal deformation due to shear and tensile faults in a half-space, *Bull. Seism. Soc. Am.*, **82**, 1018–1040.

Omuralieva, A.M., Hasegawa, A., Matsuzawa, T., Nakajima, J. & Okada, T., 2012. Lateral variation of the cutoff depth of shallow earthquakes beneath the Japan Islands and its implications for seismogenesis, *Tectonophysics*, **518-521**, 93-105.

Parsons, T., Sleep, N.H. & Thompson, G.A., 1992. Host rock rheology controls on the emplacement of tabular intrusions: Implications for underplating of extending crust. *Tectonics*, **11**, 1348-1356.

Pollitz, F.F. & Sacks, I.S., 2002. Stress triggering of the 1999 Hector Mine Earthquake by transient deformation following the 1992 Landers Earthquake, *Bull. Seism. Soc. Am.*, **92**, 1487-1496.

Prejean, S., Ellsworth, W., Zoback, M. & Waldhauser, F., 2002. Fault structure and kinematics of the Long Valley Caldera region, California, revealed by high-accuracy earthquake hypocenters and focal mechanism stress inversions, *J. Geophys. Res.*, **107**, B12, 2355, doi:10.1029/2001JB001168.

Ranalli, G., 1995. Rheology of the Earth, 2nd Edition, Chapman & Hall, London.

Rubin, A.M., 1993. Dykes vs diapirs in viscoelastic rock, *Earth Planet Sci. Lett.*, **117**, 653-670.

Rubin, A.M., 1995. Propagation of magma-filled cracks, *Annu. Rev. Earth Planet. Sci.*, **23**, 287-336.

Scholz, C.H., 1988. The brittle-plastic transition and the depth of seismic faulting, *Geol. Runds.*, **77**, 319-328.

Scholz, C.H., 1998. Earthquakes and friction laws, *Nature*, **391**, 37-42.

Sibson, R.H., 1986. Earthquakes and rock deformation in crustal fault zone, *Annu. Rev. Earth Planet. Sci.*, **14**, 149-175.

Segall, P., 2016. Repressurization following eruption from a magma chamber with a viscoelastic aureole, *J. Geophys. Res.*, **121**, 8501-8522, doi: 10.1002/2016JB013597.

Segall, P., 2019. Magma chambers: what we can, and cannot, learn from volcano geodesy. *Phil. Trans. R. Soc.*, **A 377**, 20180158, http://dx.doi.org/10.1098/rsta.2018.0158.

Takahashi, H., Ohzono, M., Okazaki, N., Suzuki, T. & Akita, F., 2017. Thermal gradient distribution around Kussharo caldera, Hokkaido, *Abstract of the 2017 Fall Annual Meeting of the Volcanological Society of Japan*, **B2**, 14 (in Japanese).

ten Brink, U., 1991. Volcano spacing and plate rigidity, *Geology*, **19**, 397-400.

Trasatti, E., Giunchi, C. & Bonafede, M., 2003. Effects of topography and rheological layering on ground deformation in volcanic regions, *J. Volcanol. Geotherm. Res.*, **122**, 89-110.

Troise, C., Pingue, F. & De Natale, G., 2003. Coulomb stress changes at calderas: Modeling the seismicity of Campi Flegrei (southern Italy), *J. Geophys. Res.*, **108**, 2292, doi:10.1029/2002JB002006.

Tse, S.T. & Rice, J.R., 1986. Crustal earthquake instability in relation to the depth variation of frictional slip properties, *J. Geophy. Res.*, **91**, 9452-9472.

Watanabe, T., Koyaguchi, T. & Seno, T., 1999. Tectonic stress controls on ascent and emplacement of magmas, *J. Volcanol. Geotherm. Res.*, **91**, 65-78.

Watts, A.B., 2001. Isostasy and flexure of the lithosphere, Cambridge University Press, Cambridge.

Watts, A.B. & Burov, E.B., 2003. Lithospheric strength and its relationship to the elastic and seismogenic layer thickness, *Earth Planet. Sci. Lett.*, **213**, 113-131.

Wessel, P., Smith, W.H.F., Scharroo, R., Luis, J. & Wobbe, F., 2013. Generic Mapping Tools: Improved Version Released, *EOS Trans. AGU*, **94**(45), 409-410.

Yamasaki, T., Sigmundsson, F. & Iguchi, M., 2020. Viscoelastic crustal response to magma supply and discharge in the upper crust: Implications for the uplift of the Aira caldera before and after the 1914 eruption of the Sakurajima volcano, *Earth Planet. Sci. Lett.*, **531**, 115981.

Yamasaki, T. & Houseman, G.A., 2012. The signature of depth-dependent viscosity structure in post-seismic deformation, *Geophys. J. Int.*, **190**, 769-784.

Yamasaki, T. & Kobayashi, T., 2018. Imaging a low viscosity zone beneath the Kutcharo caldera, eastern Hokkaido, Japan, using geodetic data, *Earth Planet. Sci. Lett.*, **504**, 1-

12.

Yamasaki, T., Kobayashi, T., Wright, T.J. & Fukahata, Y., 2018. Viscoelastic crustal deformation by magmatic intrusion: A case study in the Kutcharo caldera, eastern Hokkaido, Japan, *J. Volcanol. Geotherm. Res.*, **349**, 128-145.

Yamasaki, T., Miura, H. & Nogi, Y., 2008. Numerical modelling study on the flexural uplift of the Transantarctic Mountains, *Geophys. J. Int.*, **174**, 377-390.

APPENDIX A: PARAMETER DEPENDENCY OF GROUND SURFACE DISPLACEMENT AT THE CENTRE OF THE MODEL

We here further explore the dependence on the model parameters. $\Delta\zeta_u = \zeta - \zeta_u = u_z/u_{z0} - u_{zu}/u_{z0}$ at the centre of the modelled upper surface in response to instantaneous sill-like magma emplacement at the time $t = 0$, where u_z and u_{zu} are the vertical displacement for NET (non-uniform elastic thickness: $\Delta h > 0$) and UET (uniform elastic thickness: $\Delta h = 0$) models, respectively, and u_{z0} is the initial elastic uplift due to the instantaneous emplacement. The time t is normalised by the Maxwell relaxation time (τ). h_i is fixed to be 5 km.

Fig. A1 shows the dependence on the emplacement depth (d_s), for which Δh and δ are fixed to be 10 km and 5 km, respectively. The general model behaviour is the same with those shown in Fig. 4, where $\zeta = u_z/u_{z0}$ is greater and smaller than $\zeta_u = u_{zu}/u_{z0}$ for $\omega_e < \omega_s$ and $\omega_e \geq \omega_s$, respectively. The deviation $\Delta\zeta_u = \zeta - \zeta_u$ is greater for models with greater d_s. As described in Yamasaki et al. (2018), magma emplacement at shallower depths in an elastic layer predicts post-emplacement viscoelastic displacement to be smaller, because a relatively less amount of elastic strain is distributed into the underlain viscoelastic layer by the emplacement.

Fig. A2 shows $\Delta\zeta_u$ as a function of t/τ for two different values of Δh = 5 and 15 km. The general model behaviour does not change significantly. However, the models with Δh = 5 km show somewhat different behaviour. In some models where ω_e is smaller than ω_s, the post-emplacement $\Delta\zeta_u$ decreases first, which is different from the general model behaviour for Δh = 10 km, but then increases, which is similar as the general behaviour (see also Fig. 4). For smaller Δh, an amount of the initial elastic strain distributed into viscoelastic layer by magma emplacement is greater, which causes larger subsidence early in the post-emplacement period. The models with Δh = 15 km, on the other hand, follow the general behaviour as shown for Δh = 10 km.

Fig. A3 shows $\Delta\zeta_u$ as a function of t/τ for models with δ = 0, for which Δh = 10 km is adopted. The temporal behaviour itself is generally similar to those with δ = 5 km, except for the model with ω_s = 4 km and ω_e = 5 km, where ζ is greater than ζ_u later in post-emplacement period. It is obvious that an amount of the initial elastic strain distributed into the elastic layer by magma emplacement is greater for smaller δ. The lack of stress relaxation in the elastic layer causes $\Delta\zeta_u$ to be positive. However, the effect of a thicker elastic layer in the peripheral region, by which the relaxation-induced surface displacement rate is enhanced, appears early in the post-emplacement period. The lack of stress relaxation in the elastic layer increases the deviation in positive direction and decreases that in negative direction.

APPENDIX B: PARAMETER DEPENDENCY OF OVERALL DEFORMATION FIELD

Fig. B1 shows spatial distributions of $\Delta\zeta_a = \zeta - \zeta_a = u_z/u_{z0} - u_{zu}/u_{z0}$ at $t = t_{int} = \tau$ and 10τ for the viscosity η_a of UET model, where η_a is given so that the difference between NET and UET model behaviour is minimised at the deformation centre for a time interval of t_{int}. h_i =

d_s = 5 km, Δh = 10 km, δ = 5 km, and ω_s = 20 km are adopted for the investigation here, particularly focussing on the dependency on t_{int}.

For models with $t_{int} = \tau$ and $\omega_e \leq$ 20 km, a displacement anomaly in which $\Delta\zeta_a$ is negative appears concentrically with respect to the deformation centre. The anomaly peaks at r (the distance from the centre of the model) ~ $\omega_s/2$. The models with ω_e = 40 km, however, predict no significant signature of elastic thickness non-uniformity.

Models with $t_{int} = 10\tau$ also predict a region where $\Delta\zeta_a$ is negative, though the signature is little for ω_e = 40 km as similar to those for $t_{int} = \tau$ and 5τ. For ω_e = 5 and 10 km, the positive anomaly appears in the deformation centre, because the displacement difference between NET and UET models is minimised only for the time interval of t_{int}, where ζ is smaller and greater than ζ_a earlier and later in post-emplacement period, respectively.

The magnitude of the negative anomaly for $t_{int} = 10\tau$ is greater than that for $t_{int} = \tau$. Since the signature is basically induced by the viscoelastic relaxation that progresses with time, it would be more significant later in the relaxation process. The anomaly magnitude is, however, no more than ~15 % of the initial elastic uplift.

Fig. B2 shows spatial distribution $\Delta\zeta_a$ at $t = t_{int} = 5\tau$, showing the dependence on Δh by applying Δh = 5 and 15 km. $h_i = d_s$ = 5 km, δ = 5 km, and ω_s = 20 km are adopted. In any case, the negative anomaly appears at r ~ $\omega_s/2$, but it becomes insignificant for ω_e = 40 km, regardless of Δh. The available magnitude of the anomaly for Δh = 15 km is greater than that for Δh = 5 km, but again it is no more than ~15 % of the initial elastic uplift.

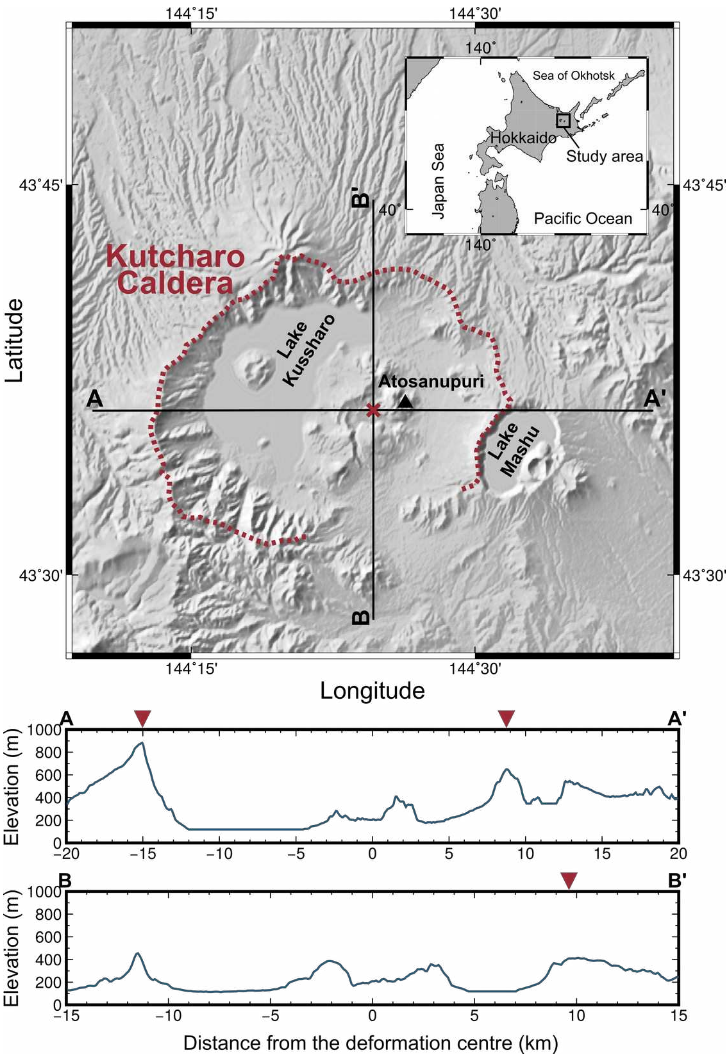

Figure 1. Location map of study area. The rim of the Kutcharo caldera (dashed red line) follows that in Fujiwara et al. (2017). The black triangle marks the Atosanupuri volcano. The red cross indicates the centre of the LOS displacement field observed by Fujiwara et al. (2017). Lower two figures show the topographic relief along the line A - A' and B - B', where the inverted triangles with red colour indicate the caldera rim. The SRTM (Shuttle Radar Topography Mission) data (e.g., Farr et al., 2007) are used for the topography.

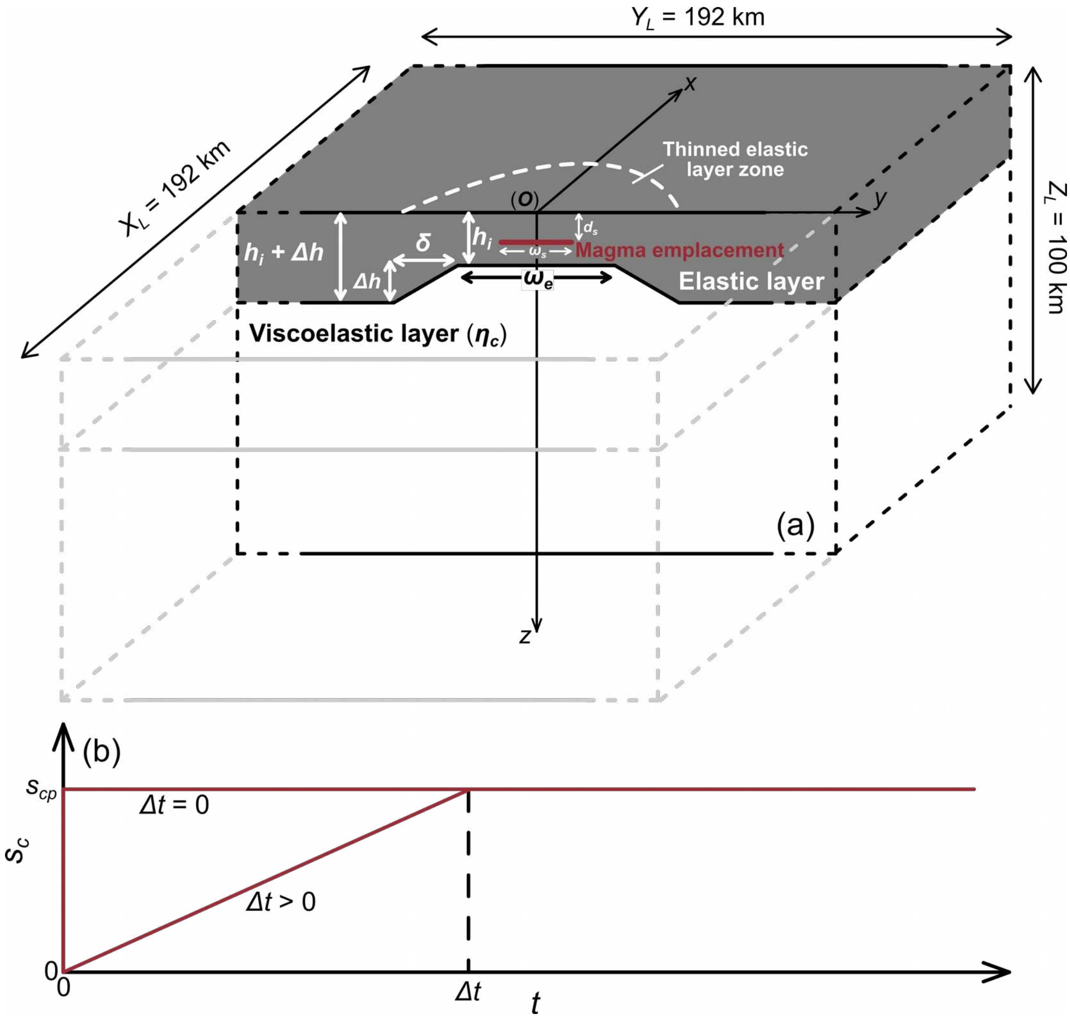

Figure 2. (a) Schematic figure of the finite element model used in this study. The modelled domain has a thickness of Z_L = 100 km, and horizontal dimensions in the *x*- and *y*-directions of X_L = 192 km and Y_L = 192 km, respectively. The axial origin (*O*) is put at the centre of the modelled upper surface. The computational solution is obtained only in the domain $x \geq 0$, for which tractions in any direction are zero on the top surface ($z = 0$), and normal displacement and tangential tractions are zero on the boundary surfaces of $x = 0$ and 96 km, $y = \pm 96$ km, and $z = 100$ km. The solution in the domain $x < 0$ is the mirror image of that in $x > 0$. The model is mechanically two-layered, i.e., an elastic layer is underlain by a viscoelastic layer with a spatially uniform viscosity (η_c). The elastic layer has an axisymmetric structure with respect to $x = y = 0$, where the thickness (h) varies with r (a horizontal distance from the model centre) as follows: $h = h_i$ for $r \leq \omega_e/2$, $h = h_i + (r - \omega_e/2)(\Delta h/\delta)$ for $\omega_e/2 < r < \omega_e/2 + \delta$, and $h = h_i + \Delta h$ for $r \geq \omega_e/2 + \delta$. A sill-like magma emplacement, whose geometry is approximated as an oblate spheroid with an equatorial radius of $\omega_s/2$, occurs at a depth of d_s. (b) Temporal change in thickness of magma emplacement. The emplacement thickness at the centre (s_c) linearly increases over a time period of Δt, and then keeps constant with $s_c = s_{cp}$ afterwards.

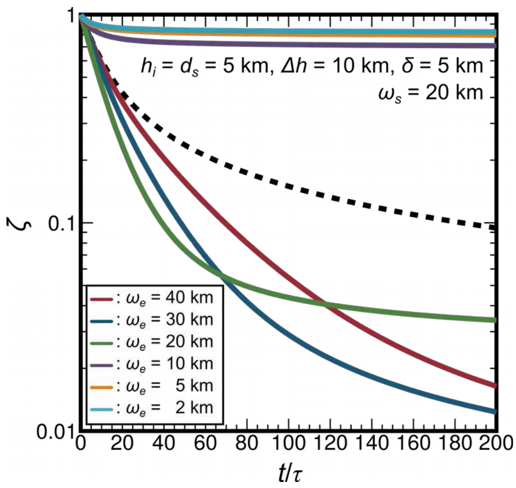

Figure 3. $\zeta = u_z/u_{z0}$ as a function of time at the centre of the modelled upper surface, where u_z is the vertical displacement for NET (non-uniform elastic thickness, i.e., $\Delta h > 0$) model, and u_{z0} is the initial elastic uplift due to instantaneous magma emplacement at t = 0, i.e., $\Delta t = 0$. The time t is normalised by the Maxwell relaxation time (τ) defined by η_c/μ, where η_c is the viscosity and μ (= 3×10^{10} Pa) is the rigidity. $h_i = d_s$ = 5 km, Δh = 10 km, δ = 5 km, and ω_s = 20 km. ω_e = (red) 40 km, (blue) 30 km, (green) 20 km, (purple) 10 km, (orange) 5 km, and (aqua) 2 km. The dashed line indicates the behaviour of UET (uniform elastic thickness, i.e., Δh = 0) model: $\zeta_u = u_{zu}/u_{z0}$, where u_{zu} is the vertical displacement for UET model.

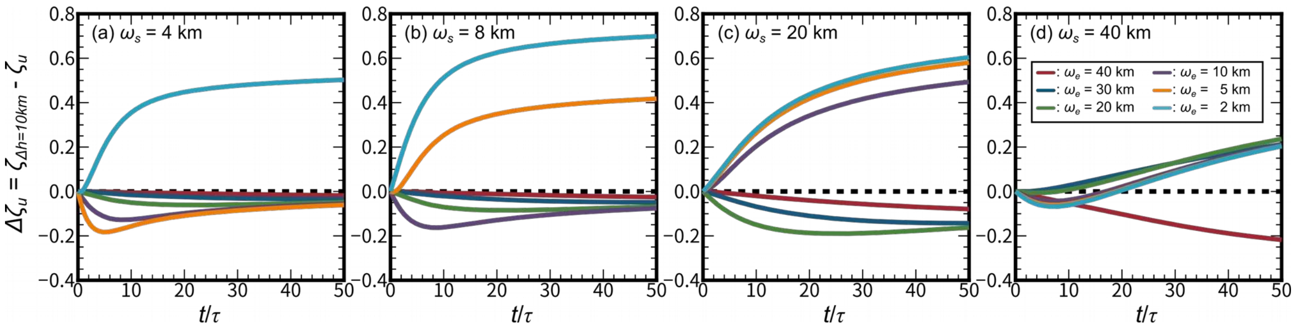

Figure 4. $\Delta\zeta_u = \zeta - \zeta_u = \zeta - u_{zu}/u_{z0}$ as a function of t/τ at the centre of the modelled upper surface. The magma emplacement occurs at $t = 0$ instantaneously, i.e., $\Delta t = 0$. $h_i = d_s = 5$ km, $\Delta h = 10$ km, and $\delta = 5$ km. ω_s = (a) 4 km, (b) 8 km, (c) 20 km, and (d) 40 km. ω_e = (red) 40 km, (blue) 30 km, (green) 20 km, (purple) 10 km, (orange) 5 km, and (aqua) 2 km. The dashed line indicates the UET model behaviour.

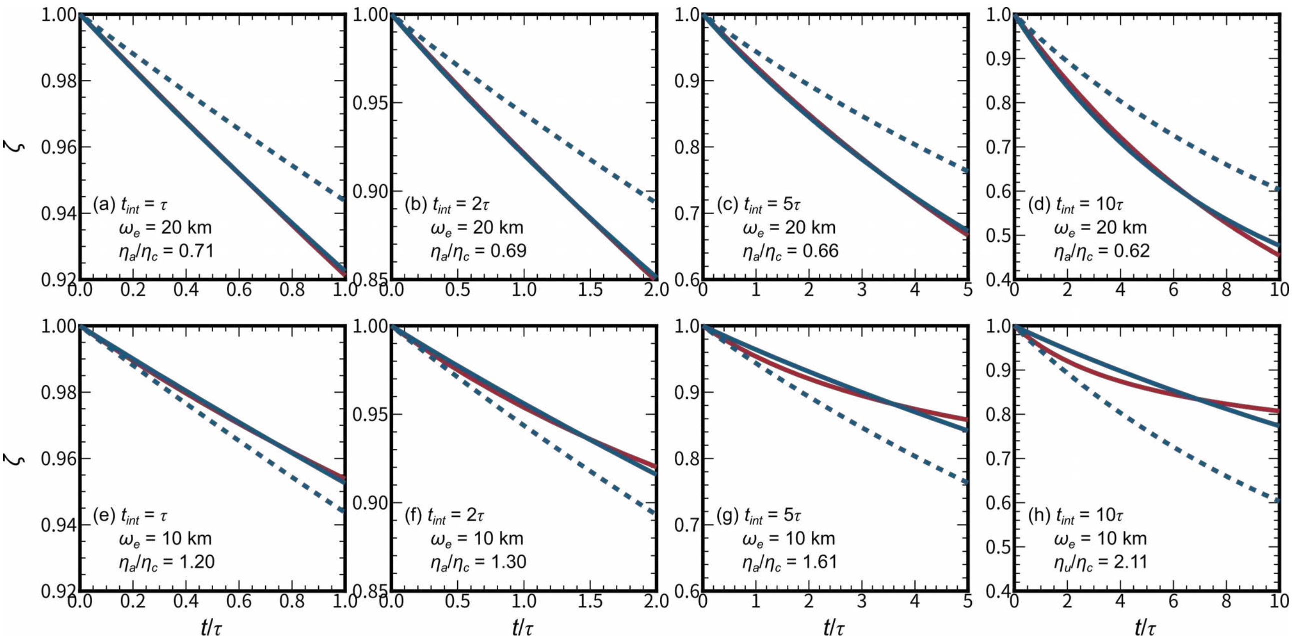

Figure 5. ζ as a function of t/τ at the centre of the modelled upper surface for (red) NET model with $\eta = \eta_c$, (solid blue) UET model with $\eta = \eta_a$, and (dashed blue) UET model with $\eta = \eta_c$, where η_a is an apparent viscosity with which the UET model best explains the NET model behaviour. t_{int} is a period over which UET model is compared with NET model to derive η_a: t_{int} = (a, e) τ, (b, f) 2τ, (c, g) 5τ, and (d, h) 10τ. ω_e = (a, b, c, d) 20 km and (e, f, g, h) 10 km. $h_i = d_s$ = 5 km, Δh = 10 km, δ = 5 km, and ω_s = 20 km.

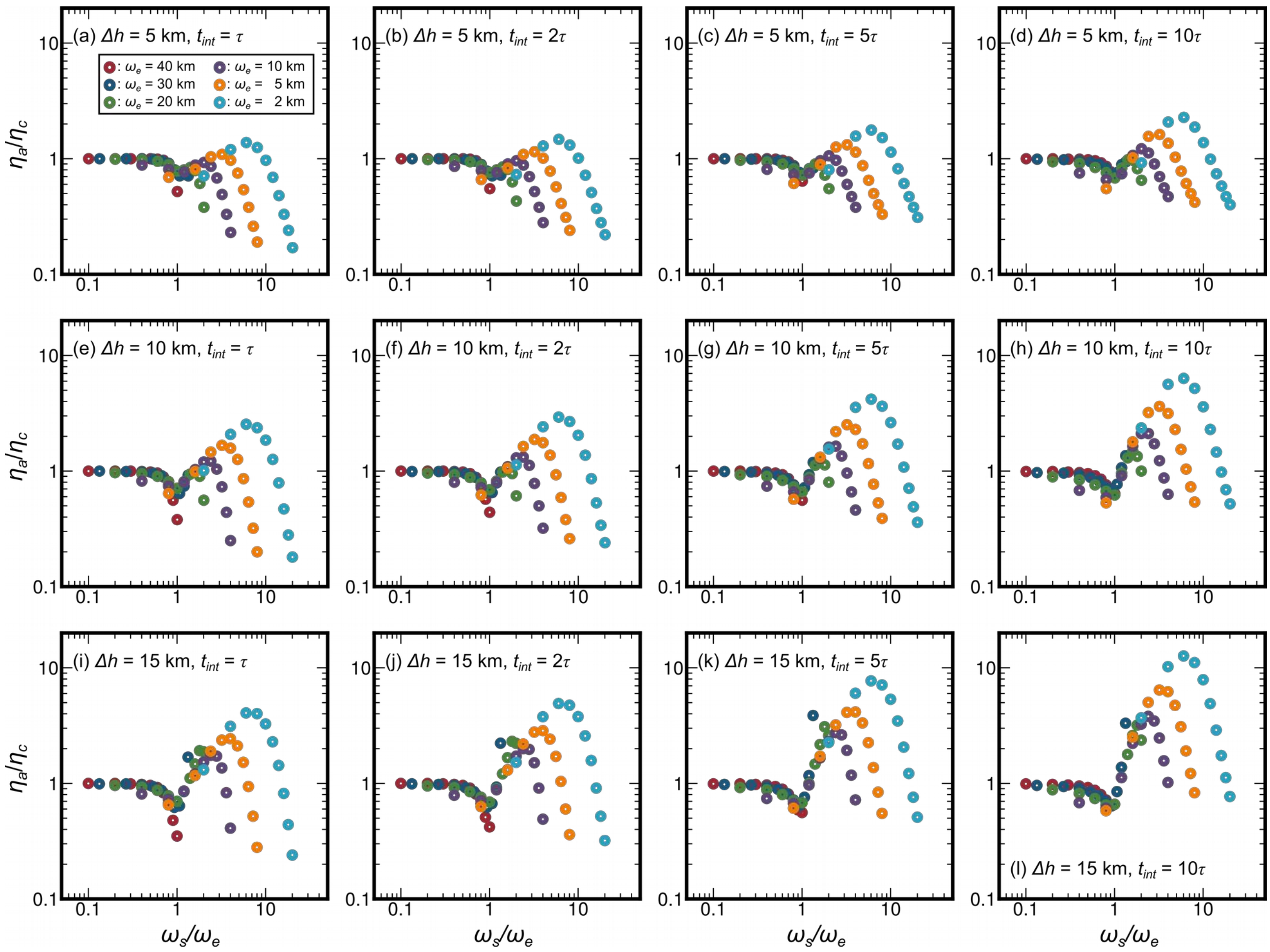

Figure 6. η_a/η_c as a function of ω_s/ω_e, where η_a is a viscosity with which the UET model best explains the NET model behaviour at the centre of the modelled upper surface for a period of t_{int}. $h_i = d_s = 5$ km and $\delta = 5$ km. Δh = (a, b, c, d) 5 km, (e, f, g, h) 10 km, and (i, j, k, l) 15 km. t_{int} = (a, e, i) τ, (b, f, j) 2τ, (c, g, k) 5τ, and (d, h, l) 10τ. ω_e = (red) 40 km, (blue) 30 km, (green) 20 km, (purple) 10 km, (orange) 5 km, and (aqua) 2 km.

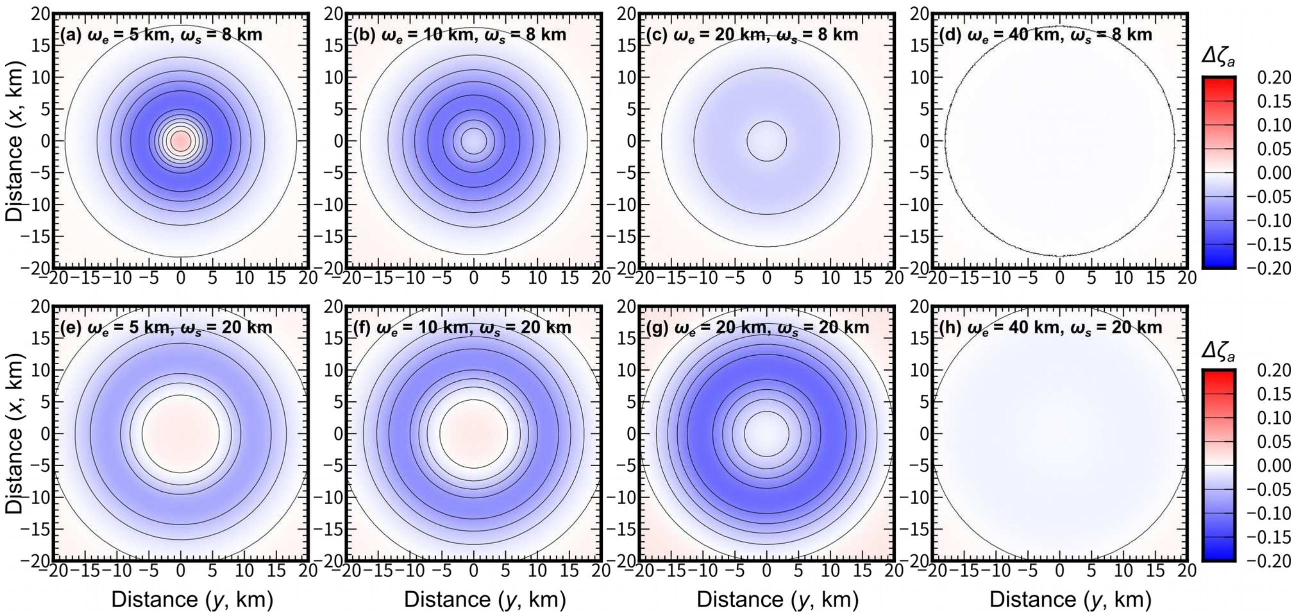

Figure 7. Spatial distribution of $\Delta\zeta_a = \zeta - \zeta_a$ on the upper surface of the model at $t = t_{int}$, where ζ_a is the vertical displacement normalised by u_{z0} for the UET model with $\eta = \eta_a$, and η_a is determined so that $\Delta\zeta_a$ is minimised at the deformation centre for the time interval $t_{int} = 5\tau$. ω_e = (a, e) 5 km, (b, f) 10 km, (c, g) 20 km, and (d, h) 40 km. ω_s = (a, b, c, d) 8 km and (e, f, g, h) 20 km. $h_i = d_s = 5$ km, $\Delta h = 10$ km, and $\delta = 5$ km. The contour interval is 0.025.

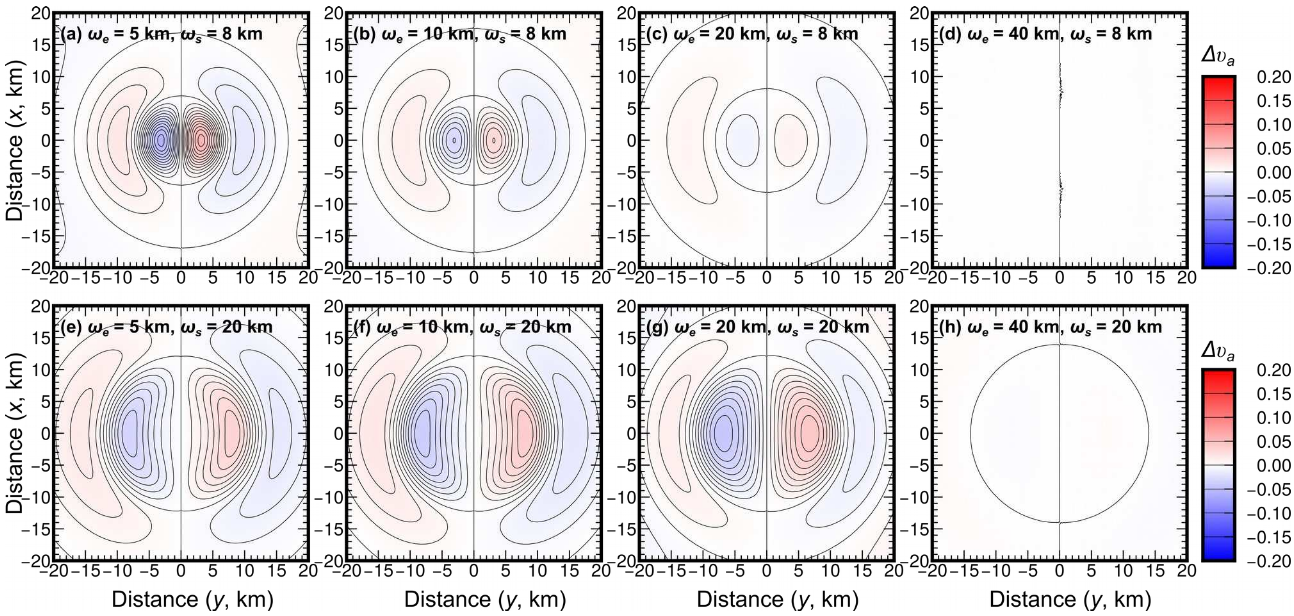

Figure 8. Spatial distribution of $\Delta\upsilon_a = \upsilon - \upsilon_a$ on the upper surface of the model at $t = t_{int}$, where $\upsilon = u_y/|u_{z0}|$ is the surface displacement in y-direction (u_y) for the NET model normalised by the initial elastic uplift $|u_{z0}|$ and υ_a is that for the UET model with $\eta = \eta_a$. η_a is determined by minimising $\Delta\zeta_a$ at the deformation centre for the time interval $t_{int} = 5\tau$. ω_e = (a, e) 5 km, (b, f) 10 km, (c, g) 20 km, and (d, h) 40 km. ω_s = (a, b, c, d) 8 km and (e, f, g, h) 20 km. $h_i = d_s$ = 5 km, Δh = 10 km, and δ = 5 km. The contour interval is 0.005.

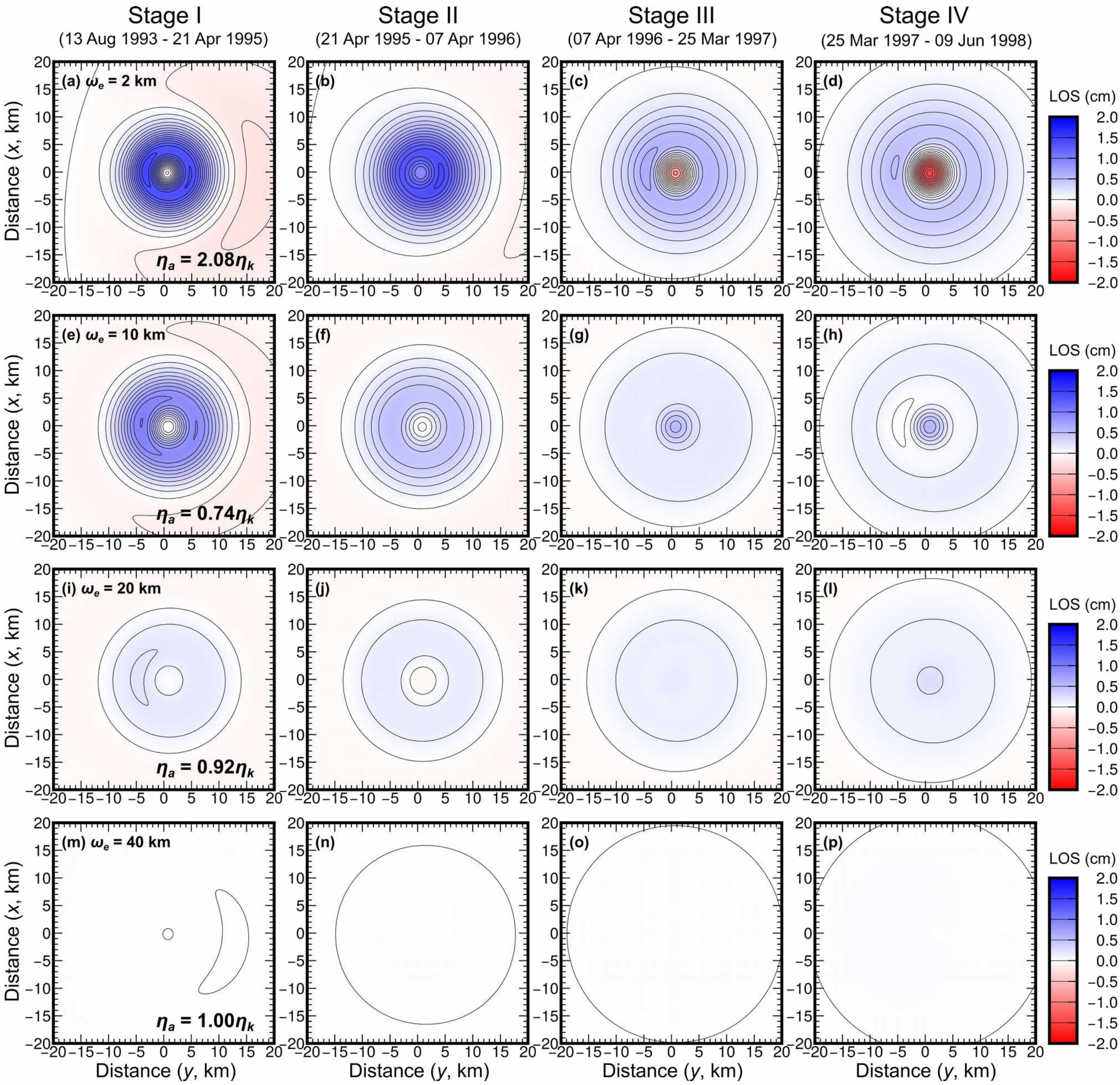

Figure 9. Difference in LOS displacement change between the NET model with $\eta = \eta_k$ and UET model with $\eta = \eta_a$ during the four different stages of (a, e, i, m) 13 August 1993 - 21 April 1995, (b, f, j, n) 21 April 1995 - 07 April 1996, (c, g, k, o) 07 April 1996 - 25 March 1997, and (d, h, l, p) 25 March 1997 - 09 June 1998, for which η_a of the UET model is determined so that the difference in post-emplacement LOS displacement change at the deformation centre is minimised over a period from 1 May 1995 to 09 June 1998. η_k = 4×10^{17} Pa s, Δt = 626 days, ω_s = 4 km, and d_s = 4.56 km; See Yamasaki et al. (2018) for the details. h_i = 5 km and Δh = 5 km (Takahashi et al., 2017; Yamasaki et al., 2018). ω_e = (a, b, c, d) 2 km, (e, f, g, h) 10 km, (i, j, k, l) 20 km, and (m, n, o, p) 40 km. δ is assumed to be 5 km. The contour interval is 0.1 cm.

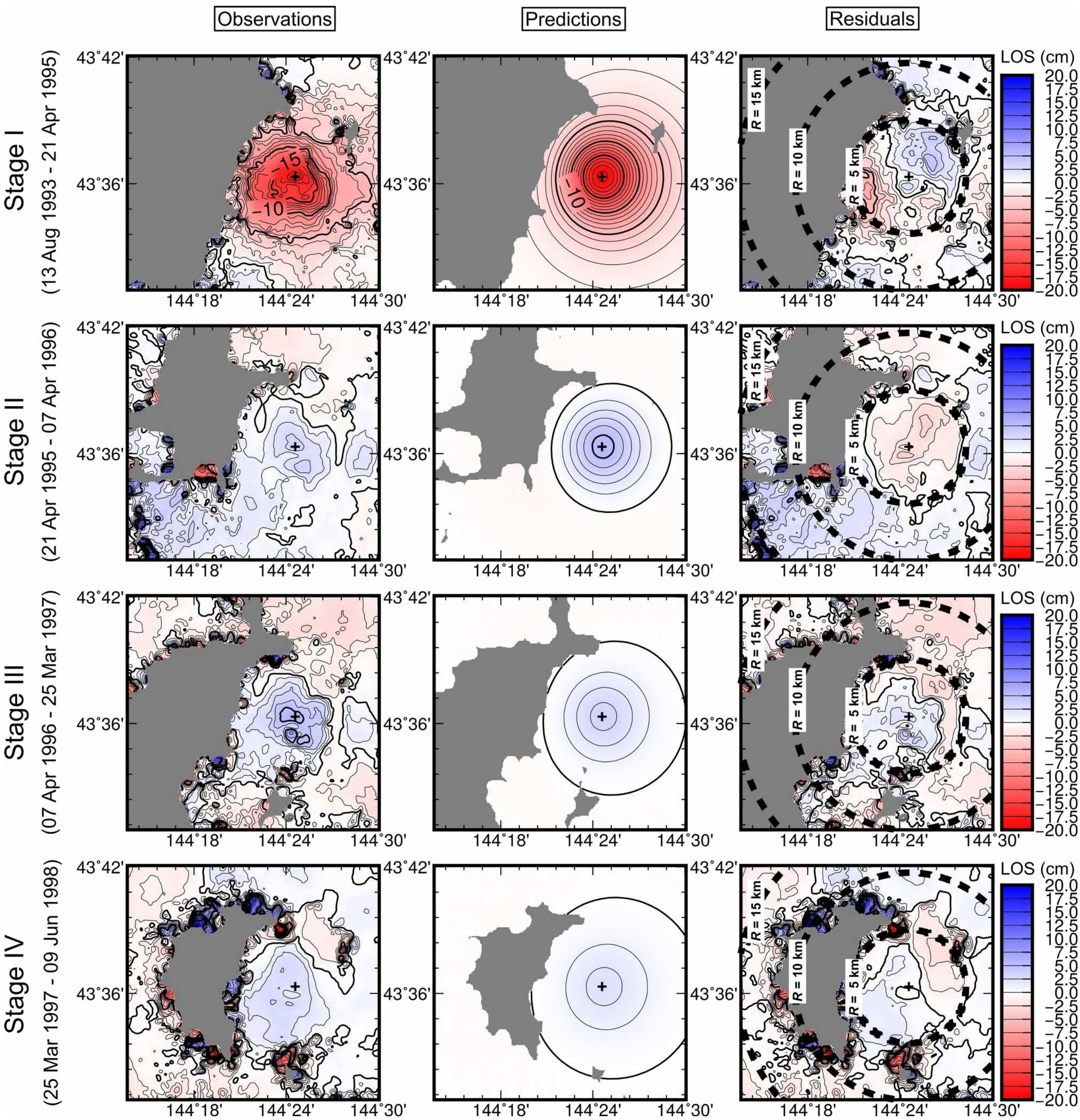

Figure 10. Observed and predicted LOS displacement changes, and the residuals, during four different stages of (I) 13 August 1993 - 21 April 1995, (II) 21 April 1995 - 07 April 1996, (III) 07 April 1996 - 25 March 1997, and (IV) 25 March 1997 - 09 June 1998. The predictions are obtained by the UET model with h_i = 5 km, Δh = 0 km, $\eta_a = \eta_k = 4 \times 10^{17}$ Pa s with which the observed post-emplacement LOS displacement is best-explained at the deformation centre (cross). ω_s = 4 km, d_s = 4.56 km, and Δt = 626 days since 13 August 1993 (Yamasaki et al., 2018). R is the distance from the deformation centre (cross). The contour interval is 1 cm.

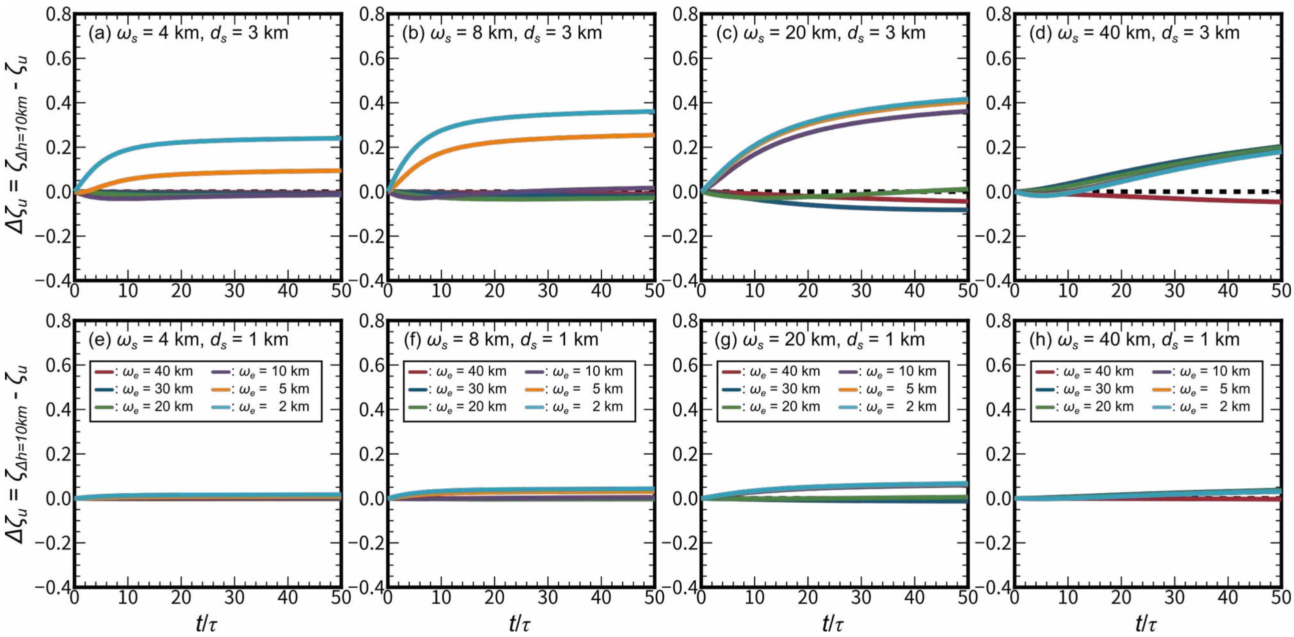

Figure A1. $\Delta\zeta_u = \zeta - \zeta_u = u_z/u_{z0} - u_{zu}/u_{z0}$ as a function of t/τ at the centre of the modelled upper surface, where u_z and u_{zu} are the vertical displacement for NET (non-uniform elastic thickness, i.e., $\Delta h > 0$ km) and UET (uniform elastic thickness, i.e., $\Delta h = 0$ km) models, respectively. t is the time, and τ is the Maxwell relaxation time defined by η_c/μ, where η_c is the viscosity and μ is the rigidity. u_{z0} is an initial elastic uplift due to instantaneous magma emplacement at $t = 0$ (i.e., $\Delta t = 0$). $h_i = 5$ km, $\Delta h = 10$ km, and $\delta = 5$ km. ω_s = (a, e) 4 km, (b, f) 8 km, (c, g) 20 km, and (d, h) 40 km. ω_e = (red) 40 km, (blue) 30 km, (green) 20 km, (purple) 10 km, (orange) 5 km, and (aqua) 2 km. d_s = (a, b, c, d) 3 km and (e, f, g, h) 1 km.

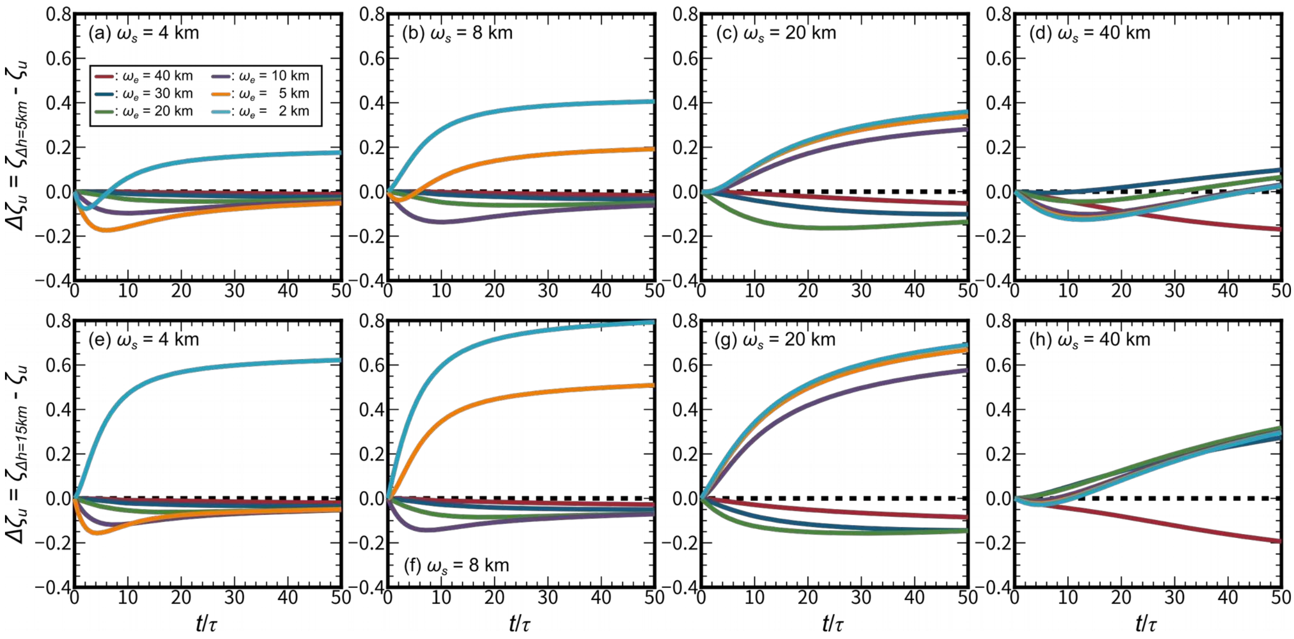

Figure A2. $\Delta\zeta_u = \zeta - \zeta_u = u_z/u_{z0} - u_{zu}/u_{z0}$ as a function of t/τ at the centre of the modelled upper surface for instantaneous magma emplacement at t = 0. $h_i = d_s$ = 5 km and δ = 5 km. Δh = (a, b, c, d) 5 km and (e, f, g, h) 15 km. ω_s = (a, e) 4 km, (b, f) 8 km, (c, g) 20 km, and (d, h) 40 km. ω_e = (red) 40 km, (blue) 30 km, (green) 20 km, (purple) 10 km, (orange) 5 km, and (aqua) 2 km.

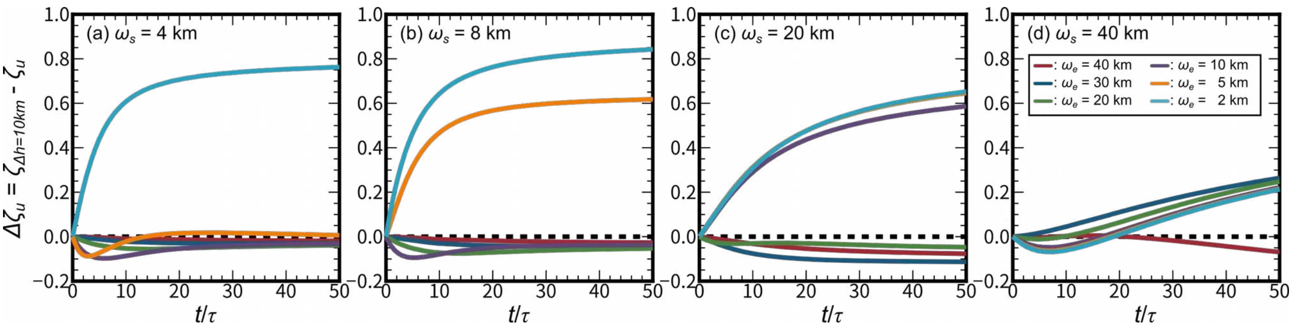

Figure A3. $\Delta\zeta_u = \zeta - \zeta_u = u_z/u_{z0} - u_{zu}/u_{z0}$ as a function of t/τ at the centre of the modelled upper surface for instantaneous magma emplacement at t = 0. $h_i = d_s$ = 5 km, Δh = 10 km, and δ = 0 km. ω_s = (a) 4 km, (b) 8 km, (c) 20 km, and (d) 40 km. ω_e = (red) 40 km, (blue) 30 km, (green) 20 km, (purple) 10 km, (orange) 5 km, and (aqua) 2 km.

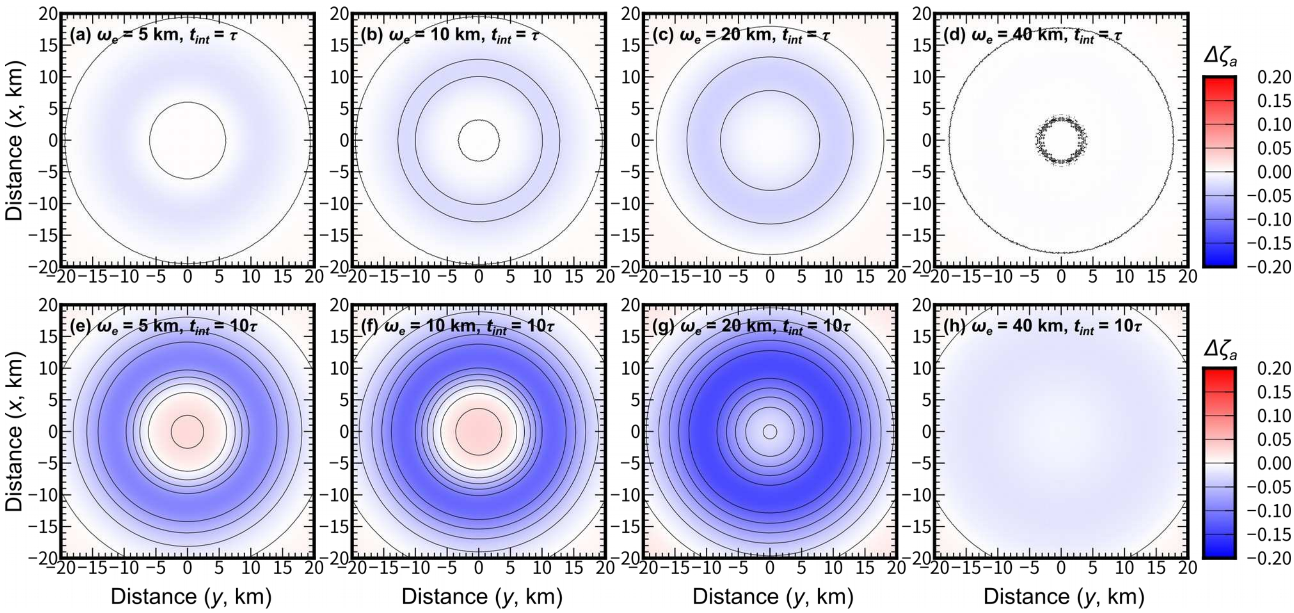

Figure B1. Spatial distribution of $\Delta\zeta_a = \zeta - \zeta_a$ on the top surface of the model at $t = t_{int}$, where the difference in vertical surface displacement between the NET model with $\eta = \eta_c$ and the UET model with $\eta = \eta_a$ is minimised at the deformation centre by adjusting η_a for the time interval t_{int} = (a, b, c, d) τ and (e, f, g, h) 10τ. ω_e = (a, e) 5 km, (b, f) 10 km, (c, g) 20 km, and (d, h) 40 km. $h_i = d_s$ = 5 km, Δh = 10 km, δ = 5 km, and ω_s = 20 km. The contour interval is 0.025.

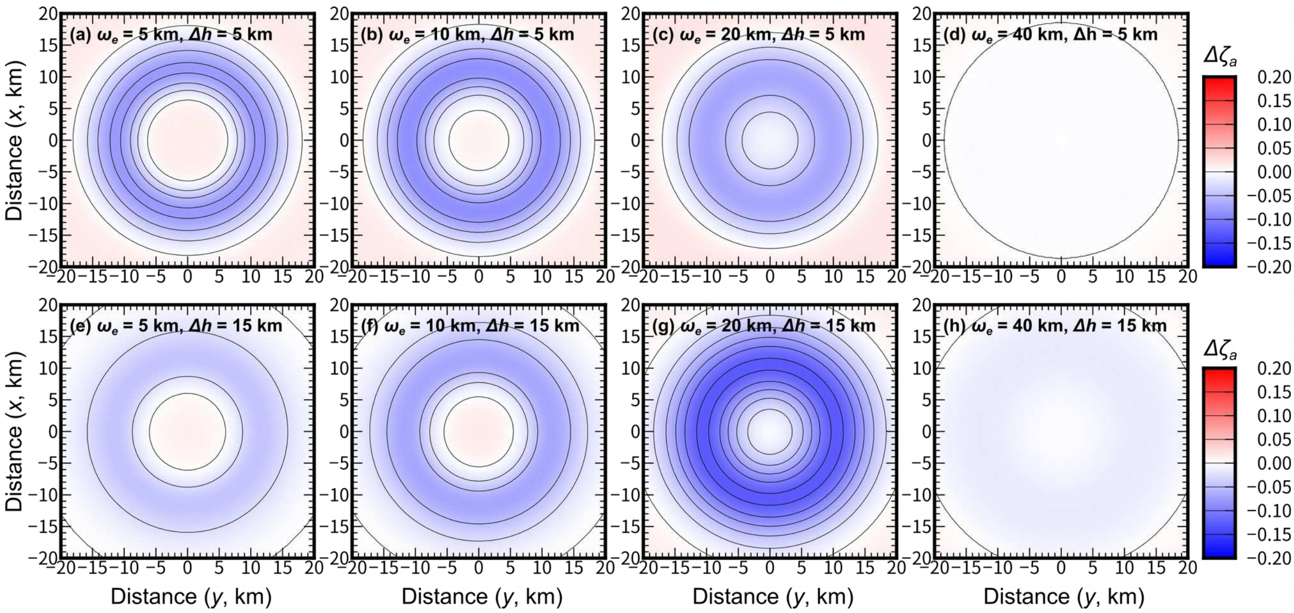

Figure B2. Spatial distribution of $\Delta\zeta_a = \zeta - \zeta_a$ on the top surface of the model at $t = 5\tau$, where the difference in vertical surface displacement between the NET model with $\eta = \eta_c$ and the UET model with $\eta = \eta_a$ is minimised at the deformation centre by adjusting η_a for the time interval $t_{int} = 5\tau$. ω_e = (a, e) 5 km, (b, f) 10 km, (c, g) 20 km, and (d, h) 40 km. Δh = (a, b, c, d) 5 km and (e, f, g, h) 15 km. $h_i = d_s$ = 5 km, δ = 5 km, and ω_s = 20 km. The contour interval is 0.025.

Table 1: Values of $\bar{\varepsilon}$ (the averaged root mean square misfit ε of the four stages) for the crustal deformation in the Kutcharo caldera

	ω_e = 2 km	ω_e = 6 km	ω_e = 10 km	ω_e = 20 km	ω_e = 30 km	ω_e = 40 km
Δh = 5 km	2.5 cm ($\eta_c = 0.47\eta_k$)	2.3 cm ($\eta_c = 1.48\eta_k$)	2.3 cm ($\eta_c = 1.29\eta_k$)	2.2 cm ($\eta_c = 1.05\eta_k$)	2.2 cm ($\eta_c = 0.99\eta_k$)	2.2 cm ($\eta_c = 0.98\eta_k$)
Δh = 10 km	2.4 cm ($\eta_c = 0.21\eta_k$)	2.3 cm ($\eta_c = 1.48\eta_k$)	2.3 cm ($\eta_c = 1.38\eta_k$)	2.2 cm ($\eta_c = 1.10\eta_k$)	2.2 cm ($\eta_c = 1.01\eta_k$)	2.2 cm ($\eta_c = 0.98\eta_k$)
Δh = 15 km	2.4 cm ($\eta_c = 0.13\eta_k$)	2.3 cm ($\eta_c = 1.35\eta_k$)	2.3 cm ($\eta_c = 1.36\eta_k$)	2.2 cm ($\eta_c = 1.12\eta_k$)	2.2 cm ($\eta_c = 1.02\eta_k$)	2.2 cm ($\eta_c = 0.99\eta_k$)

*η_c is the viscosity of NET model. $\eta_k = 4\times10^{17}$ Pa s is the viscosity of UET model and ω_s is 4 km (Yamasaki et al., 2018).